



Interactions between the MJO, Aerosols, and Convection over the Central Indian Ocean[✉]

DOUGLAS C. STOLZ, STEVEN A. RUTLEDGE, WEIXIN XU, AND JEFFREY R. PIERCE

Department of Atmospheric Science, Colorado State University, Fort Collins, Colorado

(Manuscript received 17 February 2016, in final form 8 October 2016)

ABSTRACT

This study examines covariability of boundary layer cloud condensation nuclei (CCN) concentrations [estimated using the GEOS 3D chemical transport model (GEOS-Chem)], convective clouds, precipitation, and lightning observed over the central equatorial Indian Ocean (CIO). Three distinct Madden–Julian oscillation (MJO) episodes were observed during the recent Dynamics of the MJO (DYNAMO; 2011/12) field campaign. Coherent relationships between CCN, rainfall, and lightning are apparent in time series from DYNAMO and more lightning located north of the equator is noted, compared to south of the equator. More-polluted environments north of the equator contained deep convective clouds that had stronger radar reflectivities ($\sim 2\text{--}3$ dB) in the mixed-phase region (5–10-km altitude) compared to south of the equator. Following discussion of the MJO episodes that occurred during DYNAMO, 22 cycles of the MJO observed during boreal cold seasons in the years 2004–11 are examined with the aid of TRMM satellite observations. Climatological results suggest that horizontal transport of continental aerosols from proximal landmasses by the large-scale circulation after active MJO convection reinforces the meridional gradient of CCN concentrations in the CIO. Satellite observations depicted comparable aggregate cold cloud feature area in both regions in similar thermodynamic environments, leading to the suggestion that higher CCN concentrations north of the equator act to invigorate convection. Direct comparisons of convective intensity metrics to CCN support the aerosol hypothesis; however, in line with previous studies, it is acknowledged that conditional instability, vertical wind shear, and environmental moisture can modulate the initial development of deep convection over the CIO during select phases of the MJO.

1. Introduction

The discovery of 40–50-day oscillations in the zonal winds at 850 and 150 hPa in the tropical atmosphere over 45 years ago has incited a rich interest in researching and characterizing the Madden–Julian oscillation (MJO; Madden and Julian 1971, 1972) (important acronyms in this paper are also listed and defined in the [appendix](#)). The MJO influences patterns of variability of lower- and upper-tropospheric winds, humidity, and temperature on 30–90-day time scales, and anomalies in the large-scale circulation associated with the MJO have been shown to circumnavigate the global tropics (Madden and Julian 1994; Zhang 2005). Furthermore, the MJO

has been implicated as a modulator of regional monsoon patterns, tropical cyclones, tornadoes, lightning, and extratropical weather/climate (Zhang 2013). The Dynamics of the Madden–Julian Oscillation (DYNAMO) field campaign (Yoneyama et al. 2013) took place during boreal fall and winter of 2011/12 in the central equatorial Indian Ocean (CIO). One of the overarching objectives of the field campaign was to improve understanding of the mechanisms that govern the onset and propagation of the MJO, such as the transition from shallow to deep convection (e.g., Stephens et al. 2004; Yoneyama et al. 2013).

In recent years, the impact of the MJO on atmospheric composition has received increasing attention, as the literature over multiple decades advocates a strong link between atmospheric aerosols and the microphysical and dynamical evolution of convective clouds (e.g., Tao et al. 2012; Rosenfeld et al. 2014). Observations from the Indian Ocean Experiment (INDOEX; Ramanathan et al. 2001) identified a strong meridional gradient in aerosol concentration in the CIO (e.g., Satheesh et al.

[✉] Supplemental information related to this paper is available at the Journals Online website: <http://dx.doi.org/10.1175/JAS-D-16-0054.s1>.

Corresponding author e-mail: D. C. Stolz, dstolz@atmos.colostate.edu

1998; Moorthy and Saha 2000; Ramanathan et al. 2001) and a substantial seasonal cycle related to the changing large-scale flow patterns of the Asian monsoon (Li and Ramanathan 2002). Plumes of continental aerosols observed over the CIO have been linked to transport from southern Asia and the Indian subcontinent in particular (Krishnamurti et al. 1998; Bates et al. 2002).

Previous researchers have demonstrated distinct patterns of variability in the distribution of atmospheric aerosols in association with the MJO globally, over major ocean basins, and at individual sites (Tian et al. 2008, 2011; Beegum et al. 2009; Reid et al. 2012; Guo et al. 2013; Langley DeWitt et al. 2013). Key findings from these earlier studies include a robust inverse relationship between local aerosol concentrations and rainfall, presumably due to wet scavenging, as well as notable changes in aerosol concentration, size distributions, and/or composition (e.g., Tian et al. 2008; Langley DeWitt et al. 2013) as a function of MJO phase (e.g., Wheeler and Hendon 2004). Specifically, Langley DeWitt et al. (2013) analyzed data collected onboard the Research Vessel (R/V) *Roger Revelle* during DYNAMO and found significant variations in the relative concentrations of sea salt and anthropogenic aerosols over the CIO before, during, and after peak convective activity associated with the October and November MJO episodes (2011). Fine-mode, anthropogenic pollutants were found to be abundant in the time leading up to MJO onset before being washed out as the heavy rain associated with active MJO convection developed. In the wake of active MJO convection, sea salt aerosols were shown to increase during westerly wind burst events, owing to disturbed sea states and wave breaking. The Langley DeWitt et al. (2013) study also documented several instances of aerosol concentrations reminiscent of continental conditions along the equator at 80.5°E longitude.

There is outstanding uncertainty as to 1) the reason for these episodic “outbreaks” of high aerosol concentrations on intraseasonal time scales over remote regions of the CIO and 2) whether any discernible signature of the impact of elevated aerosol concentrations on convection associated with the MJO exists. Rosenfeld et al. (2008) offered a hypothesis regarding convective invigoration and the transition from shallow to deep convection based on local variations in cloud condensation nuclei (CCN) in the subcloud layer. According to Rosenfeld et al. (2008), as clouds develop in environments with high CCN concentrations (e.g., greater than 500 cm^{-3}), the available cloud water condenses onto more nuclei, leading to more numerous droplets with smaller mean diameters. The collection of small droplets that has not been removed by the warm-rain process previously (between cloud base and the 0°C

level within the cloud) can be lofted within updrafts into the mixed-phase region of the cloud (i.e., altitudes within the cloud where the temperature ranges from approximately 0° to -40°C). Above the freezing level, subsequent riming and enhanced freezing contribute to greater release of latent heat, thereby invigorating updrafts within convective clouds. Previous investigators have inferred the occurrence of this phenomenon using observational and model-based approaches.

In a recent study of individual convective features across the global tropics, Stolz et al. (2015) noted stronger convection with increasing CCN concentrations over oceanic regions for fixed thermodynamic conditions. Nonnegligible differences in radar-observed precipitation structure occurred for relatively small increases in CCN concentrations ($100\text{--}200\text{ cm}^{-3}$) in pristine background environments, in agreement with previous investigations (e.g., Storer and van den Heever 2013; Storer et al. 2014). Thus, it is possible that even modest changes in aerosol concentrations could impact deep convective clouds associated with the initiation of MJOs over the CIO. A pressing question is whether the interaction between clouds and aerosols in the CIO is bidirectional. Previous research corroborates that the MJO’s large-scale wind anomalies affect local concentrations of atmospheric aerosols over the CIO (e.g., Langley DeWitt et al. 2013), but do these changes in atmospheric aerosol concentrations above the background pristine state influence the population of convective clouds on the basin scale?

This study builds on the findings of previous research by investigating the sources and transport of atmospheric aerosols and their subsequent impact on deep convective clouds that develop over the CIO in association with the MJO. We leverage a set of satellite and ground-based observations to study the distribution of convective clouds, their radar reflectivity structures, and lightning characteristics as they may relate to changes in atmospheric composition. Finally, we will consider the aforementioned convective cloud–aerosol interactions in the context of the background thermodynamic environments over the CIO since previous studies have documented appreciable changes in conditional instability, wind shear, and moisture throughout the life cycle of the MJO (Zhang 2005; Johnson and Ciesielski 2013; Gottschalck et al. 2013; Yoneyama et al. 2013; Rowe and Houze 2015; Xu et al. 2015).

2. Data and methodology

a. MJO indices

Many investigators have attempted to isolate intraseasonal variability within the tropics (i.e., variability

potentially associated with the MJO) by bandpass filtering atmospheric observables approximately in the 30–90-day spectral band (e.g., Kiladis et al. 2005). Citing early studies, Wheeler and Hendon (2004) noted that the leading two empirical orthogonal functions (EOFs) of bandpass-filtered single fields (i.e., outgoing longwave radiation or zonal wind) typically characterize eastward-propagating disturbances at tropical latitudes. According to Wheeler and Hendon (2004), it is possible to define a metric for determining the state of the MJO in real time [i.e., the Real-Time Multivariate MJO index (RMM index)] using the principle component time series of the leading EOF modes of outgoing longwave radiation and zonal winds at 850 and 200 hPa. Though no consensus currently exists for the optimal method to objectively define the MJO in climatology (Straub 2013; Kiladis et al. 2014), in the interest of investigating the climatological interaction of the large-scale flow, rainfall, CCN, and convective clouds, the RMM index developed by Wheeler and Hendon (2004) is chosen for the current study (time series of RMM indices are freely available via <http://www.bom.gov.au/climate/mjo/>).

b. Observations from DYNAMO 2011

The DYNAMO observations from October–December 2011 allowed for an unprecedented view of three MJO episodes using a specialized suite of radar, satellite, and surface-based instrumentation in addition to upper-air rawinsonde observations at strategic positions in an organized quadrilateral array over the CIO (e.g., Johnson and Ciesielski 2013; Yoneyama et al. 2013; Xu and Rutledge 2014). In the current study, we expand the geographical extent of the northern and southern domains relative to the DYNAMO sounding array dimensions to accommodate spatial and temporal sampling considerations of the Tropical Rainfall Measuring Mission (TRMM) satellite (6°S–6°N, 65°–85°E; Fig. 1); observations from the TRMM platform are discussed below. The spatial and temporal resolution of individual datasets varied; therefore, we chose to aggregate each data source in 6-h intervals to capture salient aspects of variability in the convective cloud population during DYNAMO. We will emphasize regional differences in the convective cloud population between the northern and southern regions (outlined geographically in Fig. 1 using red and blue solid lines, respectively).

In the initial observational component of this investigation, data from the Level 4 DYNAMO collection of upper-air soundings (Ciesielski et al. 2014; http://data.eol.ucar.edu/master_list/?project=DYNAMO) are used to compute environmental thermodynamic indices (described below) at various locations within the northern and southern sounding arrays defined by Johnson and

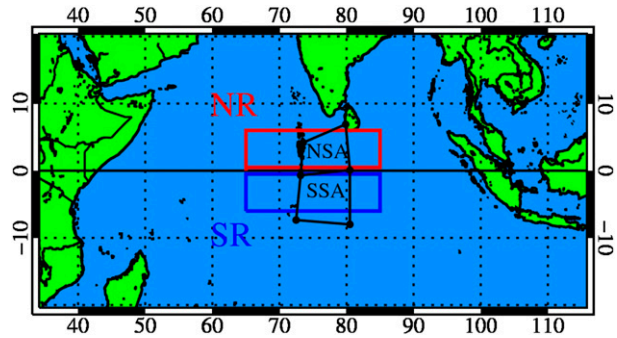


FIG. 1. The geographical domain of the central equatorial Indian Ocean spanning 20°S–20°N, 35°–115°E. The northern (NSA) and southern sounding arrays (SSA) from DYNAMO (black solid), as defined by Johnson and Ciesielski (2013) are shown in addition to the wider northern (NR; red solid; 0°–6°N, 65°–85°E) and southern (SR; blue solid; 6°S–0°, 65°–85°E) study regions chosen for this analysis.

Ciesielski (2013). In the interest of comparing environmental thermodynamic characteristics between the northern and southern study regions, we restrict our initial observation-based analysis of environmental thermodynamic sounding data to spatially disparate locations at Male Atoll in the north (4.19°N, 73.53°E) and the R/V *Mirai* in the south (8.00°S, 80.5°E). Observations from all sounding launch times are aggregated to 6-h windows surrounding 0000, 0600, 1200, and 1800 UTC by computing various thermodynamic metrics of interest and averaging over a window spanning ± 3 h around the aforementioned standard observation times.

Mixed-layer (lowest 50 hPa) pseudoadiabatic convective available potential energy (CAPE) is computed, and mixed-layer, normalized CAPE (NCAPE) is then analyzed by taking the quotient of the CAPE and the vertical distance between the level of free convection and equilibrium level (vertical distance specified in meters) in each sounding. The lifted condensation level (LCL) is approximated by multiplying the difference between a parcel's mixed-layer temperature and dewpoint temperature by a constant $c = 0.12 \text{ km K}^{-1}$ (e.g., Iribarne and Godson 1981), while the local height of the 0°C isotherm is estimated by linearly interpolating the vertical temperature profile. Warm cloud depth (WCD) (Williams et al. 2005; Carey and Buffalo 2007), or an estimate of the vertical distance over which warm-phase precipitation processes may be active, is computed by finding the vertical distance between the approximate LCL and the freezing level.

Many previous researchers have noted distinct temporal variations in vertical wind shear and environmental relative humidity over the CIO, specifically in the context of analyses of convective cloudiness in the tropics as well as in association with the MJO (Johnson

and Ciesielski 2013; Wall et al. 2014; Xu and Rutledge 2014; Rowe and Houze 2015; Xu et al. 2015). An estimate of the 6-km vertical wind shear in the environment is computed according to the magnitude of the vector difference in horizontal winds between the mixed layer and 6-km altitude above mean sea level. To study the potential impacts of environmental relative humidity/column moisture on the behavior of deep convection in the MJO, we compute the average of relative humidity between 850 and 500 hPa for each sounding.

Thermal infrared (IR) channel ($11.5\ \mu\text{m}$) observations from *Meteosat-7* are used to document the existence of cold cloud features (CCFs), defined as contiguous areas of IR brightness temperatures $T_b \leq 208\ \text{K}$. While IR T_b closer to 228 K have been optimally linked to rainfall in off-equatorial locations, such as the tropical eastern Atlantic Ocean (e.g., Arkin 1979), we are interested in studying the behavior of precipitation and lightning within deep convective clouds in the equatorial region of the CIO in response to aerosol perturbations. According to Mapes and Houze (1993), the 208-K IR T_b threshold serves as a conservative proxy for precipitating areas over deep tropical oceanic regions. The aggregate area of cold cloud for each 6-h period (using ± 3 -h windows surrounding 0000, 0600, 1200, and 1800 UTC) is defined by summing the number of *Meteosat-7* pixels within CCFs present and then multiplying the count by a 25-km^2 -pixel footprint area.

Next, we use lightning data from Vaisala's Global Lightning Dataset (GLD360) to take advantage of the continuous temporal observation capability of the dataset in light of the comparatively short duration of observations during DYNAMO. Note that Vaisala's GLD360 network detection efficiency over the CIO varied from approximately 70% at a latitude of 10°N to as low as 50% near 20°S latitude, with minimal longitudinal variations for cloud-to-ground (CG) strokes exceeding 10 kA in peak current during DYNAMO (R. Said 2016, personal communication). In the current study, we use a minimum peak current threshold of 10 kA and limit the data to events with five or more sensors reporting during classification, though we do not explicitly account for regional differences in the detection efficiency of GLD360. We bin the data geographically on a 0.5° grid and compute lightning stroke density (without grouping individual strokes to flashes) over each 6-h period (± 3 -h windows surrounding 0000, 0600, 1200, and 1800 UTC), allowing for decreasing gridbox area with increasing latitude.

Using the multisatellite merged rainfall product TRMM 3B42 (Huffman et al. 2007), basinwide rainfall characteristics are analyzed at 0000, 0600, 1200, and 1800 UTC. Areal average rainfall is computed for the

northern and southern regions by taking the unconditional average (including the presence of $0\ \text{mm h}^{-1}$ observations) of 0.25° observations from TRMM 3B42 within both the northern and southern study regions (e.g., Fig. 1) separately at a given interval. The subsequent average values for the northern and southern study regions are scaled by a factor of 6.0 (dimensionless) to arrive at an equivalent 6-hourly rainfall rate.

c. Climatological TRMM observations

Following analysis of the three individual MJO episodes in October, November, and December observed during DYNAMO, we appeal to a longer climatology of MJO events to investigate the robustness of the patterns of covariability. We focus our attention on the time spanning boreal cold seasons (October–March) for the years 2004–11 over the CIO, since the amplitude of intraseasonal variability is typically larger during these periods compared to other times of the year (Madden 1986; Zhang and Dong 2004). We choose not to include data from all months of the year for the current study in order to mitigate potential impacts of northward propagation of the MJO convective envelope and low-amplitude MJO events in composite analysis (e.g., Lau and Chan 1986; to be discussed below). Individual MJO episodes were identified by cataloging periods where the RMM phase index 1) was in phases 1–3 for a minimum of 10 days; 2) progressed from phase 6 through the peak active phases 2 and 3 (for the CIO) and then to suppressed phases 4 and 5; and 3) had a combined RMM amplitude [i.e., $(\text{RMM}_1^2 + \text{RMM}_2^2)^{1/2}$] of 1.0 or greater for at least half of the days in the cycle (time series of RMM indices are freely available via <http://cawcr.gov.au/staff/mwheeler/maproom/RMM/>). We again use the TRMM 3B42 rainfall product in order to characterize area-average rainfall characteristics for multiple MJO events in this part of our analysis (as described in section 2b). The objective of the climatological component of this analysis is to characterize the covariability between CCN, large-scale winds, and convective clouds associated with the MJO.

Because of the periodic “snapshot” observation strategy of the TRMM satellite, we analyze all available orbits intersecting the study area during cold-season months in the 8-yr period (2004–11). We use total lightning observations from the TRMM Lightning Imaging Sensor (LIS) (e.g., Boccippio et al. 2000; Cecil et al. 2014) to study the large-scale pattern behavior of lightning using the full field of view of LIS in any given orbit. For the climatological segment of the analysis, the number of flashes and the estimated time that any given scene is in TRMM's field of view (termed “viewtime”) are aggregated each day at the LIS instrument's native

0.5° resolution. Following Cecil et al. (2014), we effectively smooth total lightning flash counts and viewtime using a Gaussian kernel (of 2.5° width in the horizontal dimensions and of 111-day width in the time dimension, respectively) prior to computing flash-rate statistics. To compute daily flash rate, we multiply the quotient of the observed flash count and viewtime by a conversion factor ($86\,400\text{ s day}^{-1}$).

To study the behavior of individual convective events with respect to CCN and environmental factors, we adopt the convective precipitation feature (CF) grouping scheme (e.g., Nesbitt et al. 2000; Liu et al. 2008), thereby restricting radar data to contiguous areas of convective precipitation from the TRMM precipitation radar (PR) and any attributed lightning information. For the subset of individual lightning-producing CFs (LPCFs), the number of convective precipitation pixels, the total lightning flash count, and the LPCF's viewtime are catalogued. The flash rate is defined by the quotient of the flash count and the viewtime, and, subsequently, total flash density (TLD) is computed by normalizing the flash rate by the product of the number of convective PR pixels and a constant footprint area of 25 km^2 following the TRMM satellite's boost maneuver in 2001. In addition, we adopt a metric that takes the average behavior of the 30-dBZ echo-top height (AVGHT30) within individual CFs into account (Stolz et al. 2015).

We study the collection of individual vertical profiles of radar reflectivity (VPRR) from the TRMM PR 2A25 orbital data (Kummerow et al. 1998; Iguchi et al. 2000) to document regional variations in vertical precipitation structure. The TRMM PR 2A25 algorithm reproduces information from the 2A23 rain characteristics algorithm (i.e., rain type, the presence of a stratiform bright band, and the presence of warm rain), and we isolate deep convective VPRRs using the 2A23 convective–stratiform rain-type flag and various maximum altitude thresholds for the 30-dBZ echo top within each profile. General reference to deep convective CFs and VPRR throughout the text that follows refers to CFs and VPRR that have been subjected to a minimum of a 5-km 30-dBZ echo-top height threshold.

We attribute estimates of environmental CCN concentrations and thermodynamic factors to each CF by averaging CCN data from a chemical transport model within an upstream inflow swath and from the nearest reanalysis gridpoint sounding, respectively. Each VPRR is matched to the nearest neighboring grid point in the chemical transport model to investigate potential differences in precipitation characteristics with respect to CCN. Data from the GEOS 3D chemical transport

model (GEOS-Chem) and reanalysis products are described next.

d. GEOS-Chem and MERRA data

For both the DYNAMO period and the climatological analysis, we utilize data from a chemical transport model, GEOS-Chem (www.geos-chem.org) with the online Two-Moment Aerosol Sectional (TOMAS) microphysics module (Adams and Seinfeld 2002; Pierce and Adams 2009; D'Andrea et al. 2013; Pierce et al. 2013), to simulate the number concentration of aerosols with diameters greater than or equal to 40 nm (N40) across a domain spanning the Indian Ocean and portions of adjacent continents [20°S – 20°N , 35° – 115°E ; see Stolz et al. (2015) and references therein for a detailed discussion of model design and uncertainty]. N40 is assumed to be an appropriate proxy for the number concentration of CCN in convective clouds with a peak supersaturation of $\sim 1\%$ (Dusek et al. 2006). In addition, we assume that the spatial and temporal variability of CCN in the lower troposphere is adequately characterized by the relatively coarse resolution used in the model (roughly 200 km in the horizontal, 10 vertical levels between 1000 and 850 hPa). Note that the difference between modeled and observed values of N40 was shown to be less than a factor of 1.17, on average, for comparisons between GEOS-Chem and multiple ground stations between North America and Europe (D'Andrea et al. 2013). Plumes of continental aerosols have been shown to exist primarily in layers extending up to 400–3000 m above the ocean surface in remote regions of the Arabian Sea, Bay of Bengal, and the tropical Indian Ocean (Satheesh et al. 1999; Ramanathan et al. 2001). Hence, we represent CCN for our study by the boundary layer average for 1000–850 hPa.

Background thermodynamics and low-level winds (1000–850-hPa average) derived from the Modern-Era Retrospective Analysis for Research and Applications (MERRA; <http://gmao.gsfc.nasa.gov/merra/>) are analyzed at 0000, 0600, 1200, and 1800 UTC and subsequently averaged over each full day in the current study (note that the MERRA product was chosen specifically to ensure that the low-level wind fields were as consistent as possible between GEOS-Chem and the reanalysis). The horizontal components of the low-level wind and mixed-layer (lowest 50 hPa) pseudoadiabatic CAPE are analyzed for each day in the aforementioned cold-season months in the years 2004–11 over the CIO domain. The mean values of reanalysis CAPE for the northern and southern regions during DYNAMO agreed well with observations shown by Ciesielski et al. (2014), but appreciable variability in the temporal evolution between regions is noted, and these details will be

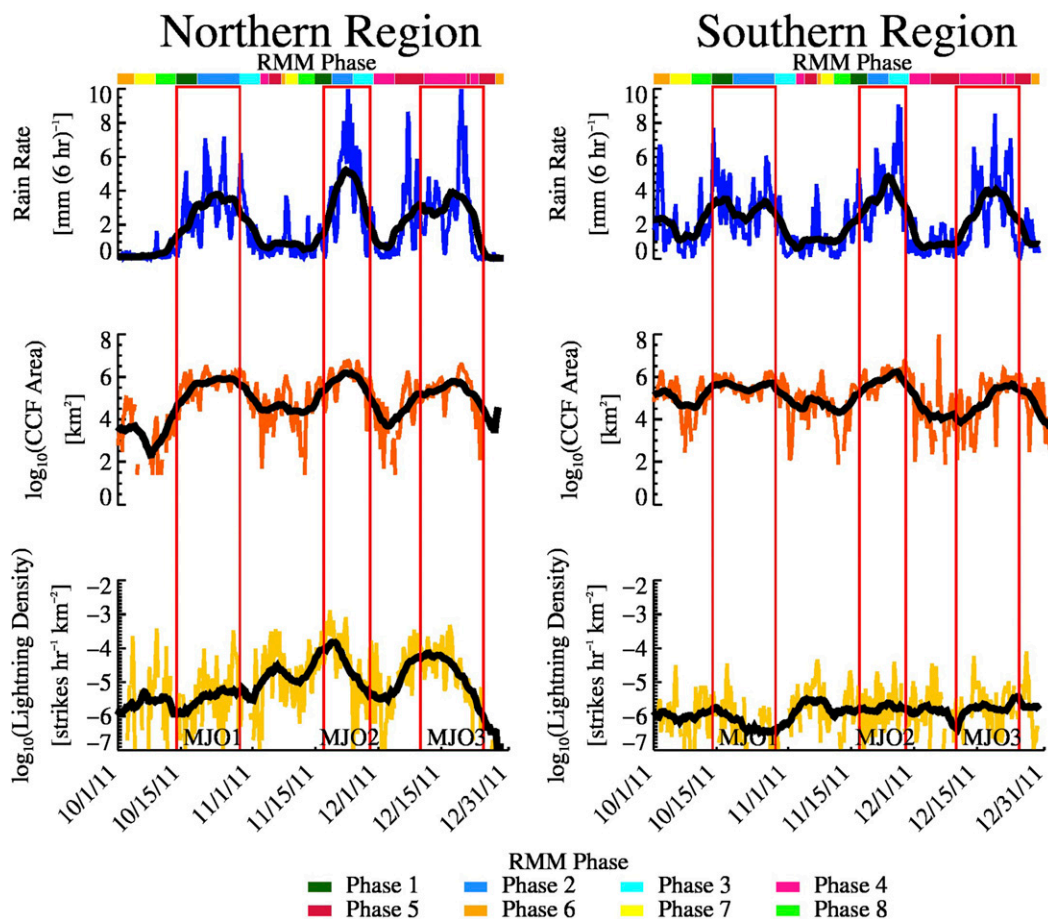


FIG. 2. Time series of (top) TRMM 3B42 rain rate (blue solid), (middle) base-10 logarithm of the aggregate area of cold cloud features (orange solid), and (bottom) base-10 logarithm of GLD360 lightning stroke density (yellow solid) from 1 October to 31 December 2011 over the (left) northern and (right) southern study regions, as well as the three MJO periods that were documented in DYNAMO (vertical red solid bars). Thick black solid lines represent the 29-time-step (1 week) boxcar average. The RMM phase is delineated at the top of each panel for reference, with color classifications for each RMM phase shown in the bottom legend.

discussed in a subsequent section. Normalized CAPE, 6-km shear, midlevel relative humidity, and warm cloud depth were computed in a manner analogous to the methodology applied to observations that is described in section 2b.

3. Results

a. Observations from DYNAMO

To begin, we analyzed the simultaneous evolution of rainfall, CCFs, lightning, and environmental factors for the three MJO episodes observed during DYNAMO. The results are succinctly summarized via time series of TRMM 3B42 rainfall, the aggregate area of *Meteosat-7* CCFs ($<208\text{ K}$), and lightning stroke-rate densities in Fig. 2, as well as time series of boundary layer average

CCN, relative humidity, shear, warm cloud depth, and mixed-layer NCAPE over both the northern and southern regions. Gridded data for 3B42 rainfall and boundary layer CCN from GEOS-Chem have been spatially averaged within the northern and southern study regions at each time step as detailed in section 2 above. In addition, each time series (colors) has been smoothed using a 29-time step (1 week) boxcar running mean (thick, black solid) to gain insight about variations on longer time scales (i.e., at lower frequencies).

MJO-like episodes are clearly evident (labeled MJOs 1, 2, and 3, for the October, November, and December events, respectively) in both the northern and southern regions according to variations in TRMM 3B42 rainfall (e.g., Xu and Rutledge 2015) and CCF observations in both regions. For MJO3, outgoing longwave radiation anomalies and average rainfall distributions reminiscent

of typical MJO episodes were apparent, but progressive large-scale pattern behavior, in terms of the RMM diagnostics, was not observed for the late December event (Gottschalck et al. 2013; Yoneyama et al. 2013). Lightning occurs more frequently in the northern region compared to the southern region, and it is evident that peaks in lightning density occur just prior to peaks in heavy rainfall (especially in the northern region). Note that, during periods of peak electrical activity observed by GLD360, the north–south difference in lightning is in excess of a factor of 10 such that a maximum decrease in detection efficiency in the meridional direction across the CIO region of up to 20% would not account for the regional differences in lightning that are observed in this study. We note that the aggregate cold cloud area (middle panels in Fig. 2) is very similar between the northern and southern regions over the course of the DYNAMO-observed MJOs, yet the bulk of the lightning occurs in the northern region.

In Fig. 3, boundary layer CCN concentrations vary on MJO time scales (perhaps in relation to the MJO itself), and CCN concentrations are overall markedly higher in the northern region compared to the southern region. Peak CCN concentrations in the northern region exceed 500 cm^{-3} , while peak CCN concentrations in the southern region rarely exceed 100 cm^{-3} . In line with previous studies, moisture in the middle troposphere (second panels, magenta solid) tends to reach its peak values in the midst of active MJO conditions with significant variations noted both between the sounding site at Male Atoll and aboard the R/V *Mirai* as well as in between individual MJO episodes at a given location. WCD tracks near-surface moisture characteristics of the environment, and it is clear from Fig. 3 that periods of enhanced convection tend to occur coincident with deeper WCD (or more moisture present in the lower troposphere) in both regions, though the environment at Male Atoll in the northern region is slightly drier (WCD is about 100 m shallower) than the environment over the R/V *Mirai* on average. The time series for the shear vector over the lower to middle troposphere at Male Atoll [third panel of Fig. 3 (left), orange solid] depicts distinct periodicity, with the highest shear occurring toward the peak of convective activity associated with MJO1 and MJO2 (data for MJO3 are absent, but a similar trend can be observed). At the R/V *Mirai*, periodic variations in the time series of the 6-km shear vector are less apparent, but peak values of wind shear are generally realized around times of active deep convection associated with the MJO. There is little evidence of MJO modulation of NCAPE at either of the two sounding locations with the exception of higher NCAPE in suppressed periods

associated with increasing sea surface temperature prior to heavy rain periods, especially leading up to MJOs 1 and 2 (Xu and Rutledge 2014).

The time series presented in Figs. 2 and 3 suggest that CCN are rapidly depleted because of washout (note the quadrature relationship of the rainfall and CCN time series in the top panels of each figure, respectively, in both the northern and southern regions) as the heavy MJO rain sets in, consistent with Langley DeWitt et al. (2013). A subtle, yet important, aspect of the covariability between rainfall, lightning, NCAPE, moisture, and CCN is that CCN concentrations are diminishing (in the domain-average sense) as lightning activity increases, presumably associated with isolated, deep convection (via wet deposition during convective precipitation), prior to the onset of widespread rainfall (Xu and Rutledge 2014). However, CCN concentrations north of the equator during these periods of enhanced lightning still tend to be greater by a factor of 2 or more than what is typically observed in pristine oceanic regions (e.g., Heintzenberg et al. 2000; Spracklen et al. 2011). Hence, we suggest that the temporal intersection of increasing NCAPE and humidity, sufficient for the development of deep convection, and higher CCN concentrations observed in the northern region (compared to the southern region) are perhaps acting to enhance convection locally via the invigoration mechanism proposed by Rosenfeld et al. (2008).

Cecil et al. (2014) illustrated a distinct north–south gradient in total lightning flash-rate climatology over the CIO using observations from multiple satellite lightning detectors (note that we also computed the lightning climatology for 2004–11 using LIS data, and our results were consistent with the earlier study by Cecil et al.). Therefore, this motivated us to explore the geographical dependence of the relationships apparent in the previous time series analysis of convective characteristics, rainfall, CCN, and lightning. For example, in the periods leading up to peak rainfall in MJOs 2 and 3 during DYNAMO, similar populations of CCFs were present in each region, yet lightning was found to occur almost exclusively in the northern region, where CCN concentrations were appreciably higher (Fig. 4).

In any given 6-h interval, the lightning density in the northern region versus the southern region differed by about an order of magnitude on average. Note that, for the period leading up to MJO1, the difference in lightning between the northern and southern regions is apparent, but the rates in both regions are small compared to observations in subsequent MJO episodes (i.e., MJO2 and MJO3). Comparison of the large-scale aerosol transport in the top panels of Fig. 4 illustrates that the low-level circulation associated with the winter monsoon was not yet established prior to MJO1, suggesting

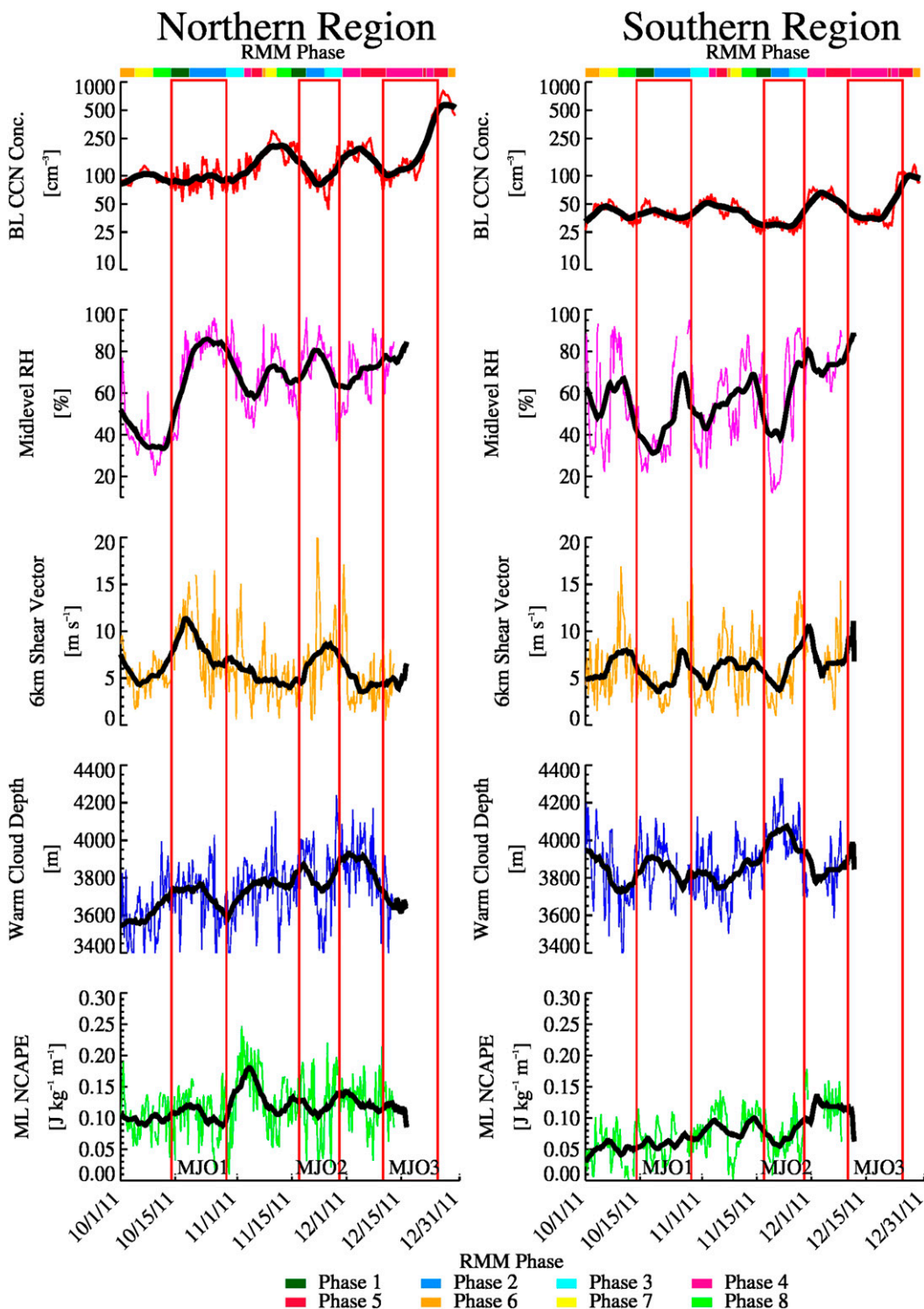


FIG. 3. As in Fig. 2, but for (top) time series of area-average predictions of CCN from GEOS-Chem (red solid). Sounding data from Male Atoll, Maldives (northern region; 4.19°N, 73.53°E), and the R/V *Mirai* (southern region; 8.00°S, 80.5°E) were used to compute (second row) midlevel (850–500-hPa average) RH (magenta solid), (third row) 6-km shear vector (orange solid), (fourth row) warm cloud depth (blue solid), and (bottom) mixed-layer NCAPE (green solid). See text in section 2 for descriptions of computation methodology.

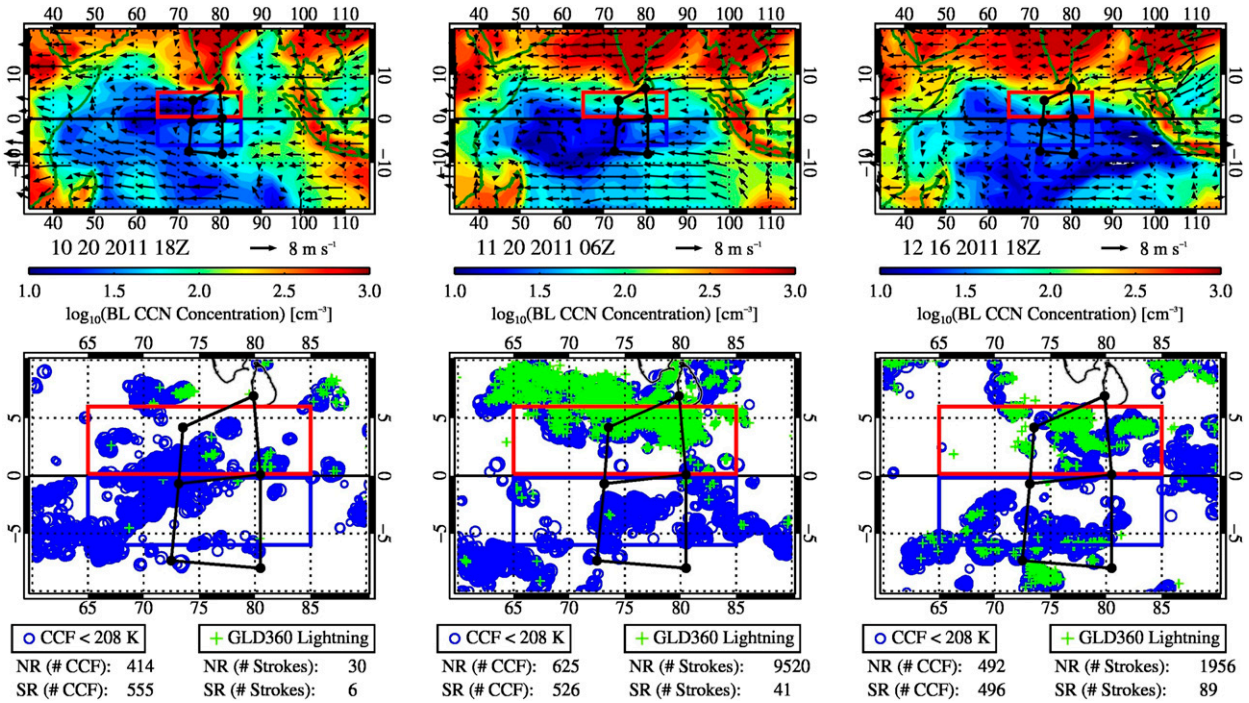


FIG. 4. The 6-h predictions of (top) boundary layer average CCN (shading; logarithmic scale) and 1000–850-hPa average wind (black vectors) vs aggregate observations of (bottom) CCFs [blue circles; size of circle is proportional to \log_{10} of the CCF area (km^2)] and GLD360 lightning (green plus signs) over the central equatorial Indian Ocean leading up to (left) MJO 1 (October), (center) MJO 2 (November), and (right) MJO 3 (December). The numbers of CCFs and lightning strokes have been tabulated for the northern and southern regions, respectively, in each region. Black solid lines denote the northern and southern sounding arrays from Johnson and Ciesielski (2013), and red solid and blue solid boxes denote the northern and southern regions, respectively, utilized for the current study. Outlines of major coastlines are shown for reference, but note the change of geographical area between the top (20°S – 20°N , 35° – 115°E) and bottom (10°S – 10°N , 60° – 90°E) panels.

airmass origins in the western equatorial Indian Ocean or eastern Africa. In contrast, during the periods leading up to MJOs 2 and 3, northeasterly flow prevails in the northern region, increasing CCN concentrations locally as a result of advection from the Indian subcontinent. More-active mixed-phase processes owing to enhanced CCN concentrations (e.g., Rosenfeld et al. 2008) could then act to produce stronger electrification and more lightning (Saunders 1993).

We consulted the TRMM database of VPRR (2A25 product) for overpasses in each study region (Iguchi et al. 2000; convective rain profiles with 30-dBZ echo tops > 5 km) during suppressed and preonset periods (i.e., RMM phases 4, 5, 6, 7, 8, and 1 from Fig. 3, when CCN concentrations are generally higher than typically observed over pristine oceanic regions) to investigate potential differences in vertical precipitation structure with respect to gradients in CCN concentrations observed during DYNAMO (Fig. 5). Each convective pixel was matched to the nearest GEOS-Chem grid point, and the GEOS-Chem data were linearly interpolated to the time of the TRMM overpass.

On average, the difference between more-polluted ($\text{CCN} > 300 \text{ cm}^{-3}$) VPRR in the northern region and pristine VPRR in the southern region ($\text{CCN} < 50 \text{ cm}^{-3}$) maximizes in the mixed-phase region (5–10 km). The difference in reflectivity between polluted and pristine environments north and south of the equator, respectively, are most apparent above the freezing level and range from about 0.5 up to 2.9 dB. To investigate whether the differences in VPRR with respect to varying CCN concentrations are robust as opposed to being the result of other background factors that may vary between hemispheres over the CIO, we studied the behavior of mean VPRR in each region, respectively (Figs. 5b,c). The reflectivity differences between polluted and pristine environments are appreciable in the northern region alone, as they range from 1.0 to 2.7 dB. In the southern region, we compare VPRR in pristine environments ($\text{CCN} < 50 \text{ cm}^{-3}$) with VPRR that were associated with $\text{CCN} > 50 \text{ cm}^{-3}$. We find a subtle difference in radar reflectivity in the southern region, though the difference is less pronounced, possibly a result of the generally low CCN concentrations that are

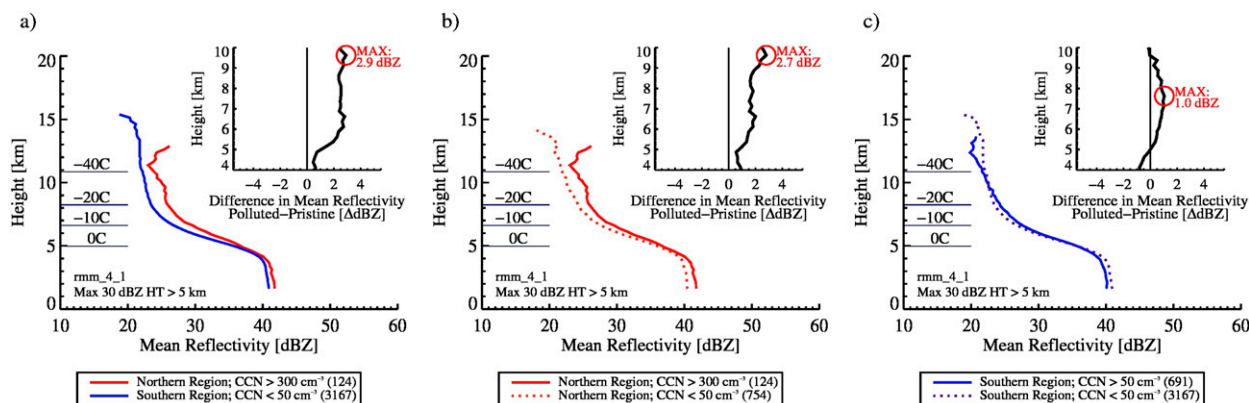


FIG. 5. The mean vertical profile of radar reflectivity for TRMM PR pixels with 30-dBZ echo-top height greater than 5 km for (a) polluted northern region vs pristine southern region, (b) polluted northern region vs pristine northern region, and (c) polluted southern region vs pristine southern region (see legend in each panel) for RMM phases 4, 5, 6, 7, 8, and 1, where the RMM amplitude exceeded 1.0 during October–December 2011. The mean height of the 0°, -10°, -20°, and -40°C isotherms within the area encompassing the northern and southern regions (6°S–6°N, 65°–85°E) have been drawn in for reference. The number of observations for each population is provided in parentheses in the legend of each panel. Differences in reflectivity in the mixed-phase region are plotted in each panel's inset; the difference is defined as the polluted reflectivity profile minus the pristine reflectivity profile in each case.

observed there (nearly 99% of VPRR observations for the southern region occurred for $\text{CCN} < 100 \text{ cm}^{-3}$). The sensitivity of these results to the chosen aerosol stratifications was investigated, and the qualitative result was found to be roughly invariant (despite limitations of decreasing sample sizes for more-polluted conditions). Here, we emphasize that variations in the vertical precipitation structure under clean and more-polluted conditions were robust between regions and within either the northern or southern region alone. These results again suggest that deep convective clouds in the CIO are more intense when they are subject to increased levels of pollutants advected from nearby continents.

Next, we investigate physical mechanisms to explain the variability of CCN concentrations in the context of the three MJO events observed during DYNAMO [i.e., potential intrusions of aerosols from nearby landmasses (e.g., Krishnamurti et al. 1998)]. According to Gill (1980), for a heat source centered on the equator (e.g., heating associated with convective precipitation during active MJO episodes), low-level, broad-scale easterlies should develop along the equator while cyclonic gyres should be manifest to the north and south of the equator, west of the heat source, in an eastward-propagating Kelvin wave–westward-propagating Rossby wave response pattern. In fact, in the time following the peak of the heavy rainfall during MJOs 2 and 3 (see the animations provided in the supplemental material), cyclonic eddies embedded within the large-scale circulation are apparent in both hemispheres. The flow pattern in the Northern Hemisphere gyre advects CCN-rich air from primarily the Middle East, India, Sri Lanka, and Indonesia into the northern region of

the DYNAMO domain. Meanwhile, the Southern Hemisphere gyre draws very clean air from the southern reaches of the Indian Ocean toward the equator, thereby establishing a sharp meridional aerosol gradient prior to the next MJO cycle.

We note that CCN concentrations over southern India and Sri Lanka frequently exceed 500 cm^{-3} , such that northerly anomalies in the meridional flow lead to a dramatic increase in CCN concentrations primarily north of the equator within our study area of interest (e.g., episodes occurring 7 November, 5 December, and 15 December 2011). Additionally, biomass burning practices throughout much of Sumatra and Kalimantan in Indonesia are known to contribute to significant increases in local concentrations of aerosols during July–November each year (Field et al. 2009). However, evidence for episodes of persistent (anomalous) easterly flow leading up to MJO onset, contributing to a meridional aerosol gradient between the northern and southern regions in the CIO, was lacking during our initial period of investigation.

According to Langley DeWitt et al. (2013), westerly wind bursts occurring in the wake of active MJO convection in DYNAMO contributed to appreciable increases in sea salt aerosols. Although we did not quantify the contributions of individual constituent aerosol species to the total estimates of CCN in the current GEOS-Chem simulations, we do not expect that continuous, local sea salt aerosol production (e.g., via wave breaking) could account for the large overall increase in the total CCN over the CIO in the wake of active MJO convection; sea salt mass is weighted toward larger particle sizes and

contributes a proportionally smaller aerosol number per mass than anthropogenic aerosols. Furthermore, the residence time of supermicron-sized sea salt aerosols is on the order of 1 day or less (fast deposition rates). We argue that circulations induced by the MJO itself appear to contribute to increases in CCN north of the equator, as low-level winds advect anthropogenic CCN from parts of the Middle East, India, and southern Asia toward the northern region of the CIO. Though the presence of small numbers of sea salt aerosols can precipitate efficient warm-rain processes in polluted environments, effectively cleansing aerosols from the lower troposphere via wet deposition (e.g., Rosenfeld et al. 2002), our results suggest that anthropogenic aerosols remain suspended in the lower troposphere during the elapsed 1-week period between RMM phases 4 and 5 and the more intense convection occurring subsequently in RMM phases 8 and 1.

Thus, we have documented apparent trends in CCN concentrations that appear to be related to large-scale circulations associated with the MJO (e.g., Fig. 3) over the CIO, and the results corroborate earlier research from INDOEX outlining the existence and seasonal variability of the large-scale hemispheric gradient in aerosol concentrations in this region (e.g., top panels of Fig. 4). We have also shown evidence that the meridional gradient in CCN concentrations over the CIO varies on intraseasonal time scales and, second, that resulting hemispheric differences in CCN concentrations impact deep convective clouds (i.e., greater radar reflectivities aloft and more lightning) in the time leading up to the initiation of subsequent MJO episodes (bottom panels of Fig. 4 and Fig. 5). Thus, our initial results are in support of the hypothesis that the MJO is responsible for modulating regional CCN concentrations in the CIO, and the impact of these CCN on subsequent cloud system development is nonnegligible. Though the relationships between aerosols and convective clouds observed were consistent for three distinct MJO episodes in our initial study, it remains to be seen whether these patterns are a robust feature of climatology for this region. To address this issue, we next turn to an investigation of climatological behavior of rainfall, radar reflectivity, lightning, and environmental factors.

b. Climatological behavior

1) PATTERNS OF RAINFALL AND CCN

Time series of the areal-average rain rates from the TRMM 3B42 product are shown for the northern and southern regions in Fig. 6 for the boreal cold seasons in the years 2004–11, with the onset of RMM phase 2 and duration of each identified MJO episode highlighted

along the abscissa. In general, the onset of RMM phase 2 relative to the peaks in the rainfall time series varies between episodes, and the rainfall observed during MJO episodes can be rather asymmetric between the northern and southern regions. For several of the identified MJO events, the rainfall amounts do not appear to differ substantially from background quiescent periods (i.e., 15 February 2007, 7 March 2010, and 13 March 2011); Kiladis et al. (2014) noted that zonal wind signatures can strongly project onto the leading two combined EOF modes of equatorial variability identified by Wheeler and Hendon (2004), leading to an inflated RMM index amplitude, even in the absence of large-scale outgoing longwave radiation anomalies. Nonetheless, 22 individual events are identified using the RMM index method, and thus there is high confidence that a sufficient sample of independent MJO episodes has been captured by our 8-yr climatology. We next question whether large-scale patterns in low-level winds (e.g., potentially those associated with the above-mentioned regional/intraseasonal variations in rainfall) affect local concentrations of CCN.

Figure 7 shows the mean geographical distribution of anomalies of CCN concentrations and anomalies of the 1000–850-hPa layer-mean wind. Note, the seasonal cycles (defined for the 2004–11 cold-season climatology) of zonal and meridional winds and CCN have been removed from the time series at each reanalysis grid point prior to computing anomalies for each RMM phase (e.g., Tian et al. 2011). In addition, anomalies for CCN and the low-level horizontal wind components are defined relative to the mean over *all days* in boreal cold-season months for 2004–11. To assess statistical significance for anomalous CCN and lower-tropospheric winds, we use a two-sample (nonparametric) Kolmogorov–Smirnov test and evaluate the relevant null hypothesis: that is, that subsets of anomalous winds or CCN concentrations in each RMM phase and underlying climatology are drawn from the same distribution. The test statistic for the two-sample Kolmogorov–Smirnov test is defined by the largest absolute difference in the cumulative density functions of each data sample (Wilks 2011). Anomalous flow vector components and anomalous CCN concentrations that are statistically significant at the 5% level according to the Kolmogorov–Smirnov test are denoted by thick black vectors and shading, respectively.

In each RMM phase, a mean meridional gradient in CCN concentrations is apparent between the northern and southern regions in the CIO (not shown), in line with observations from Ramanathan et al. (2001); however, variations in anomalous CCN concentrations throughout the different RMM phases of the MJO cycle are evident. In RMM phases 2 and 3 (Figs. 7b,c), when

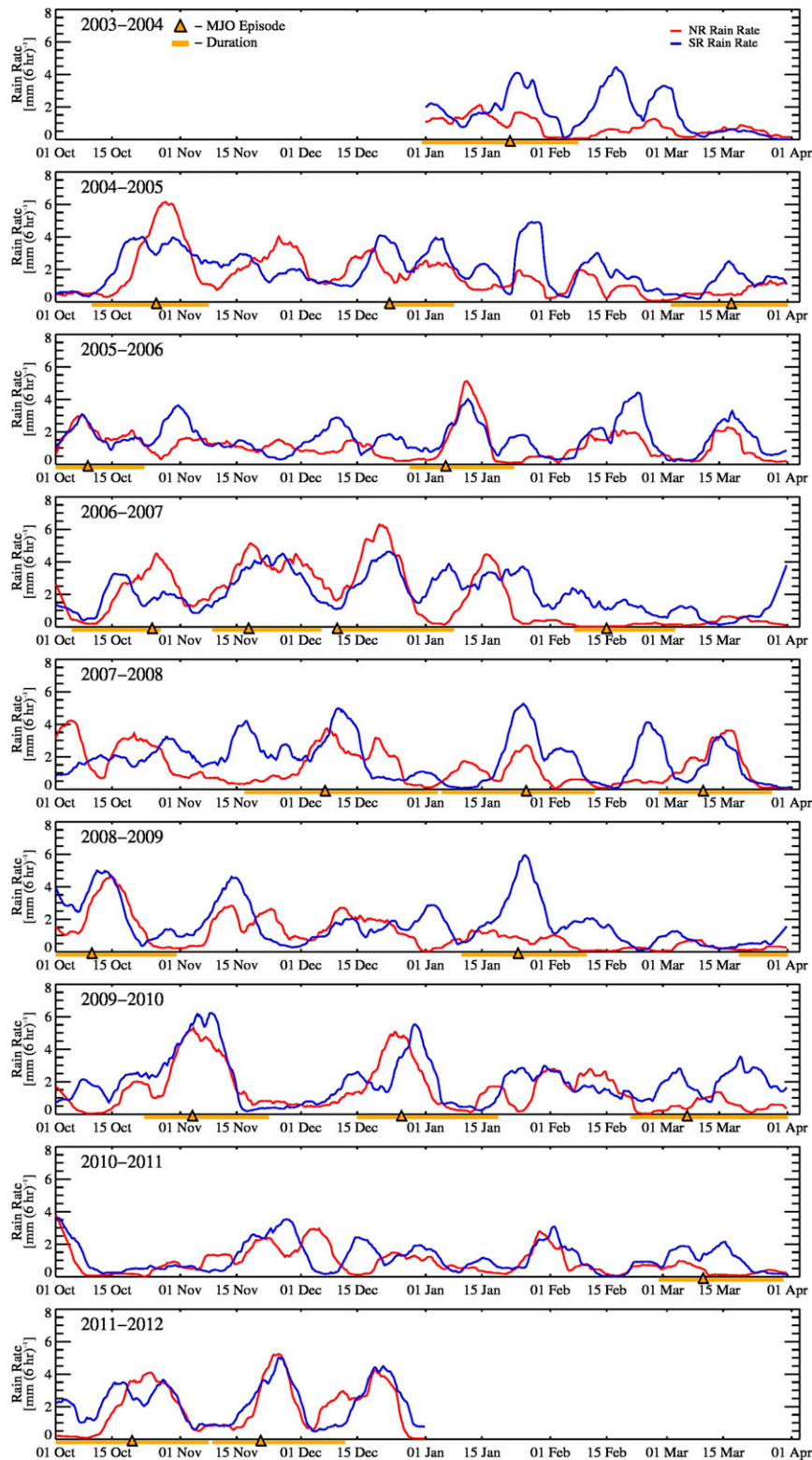


FIG. 6. Areal-average TRMM 3B42 rainfall [$\text{mm} (6 \text{ hr})^{-1}$] over the northern region (red solid) and southern region (blue solid) for nine cold seasons between January 2004 and December 2011. Rainfall time series have been smoothed using a 29-point (~ 1 week) boxcar moving average. The onset of RMM phase 2 (gold triangle with black outline) and duration (solid gold line) for identified MJO episodes are shown along the abscissa.

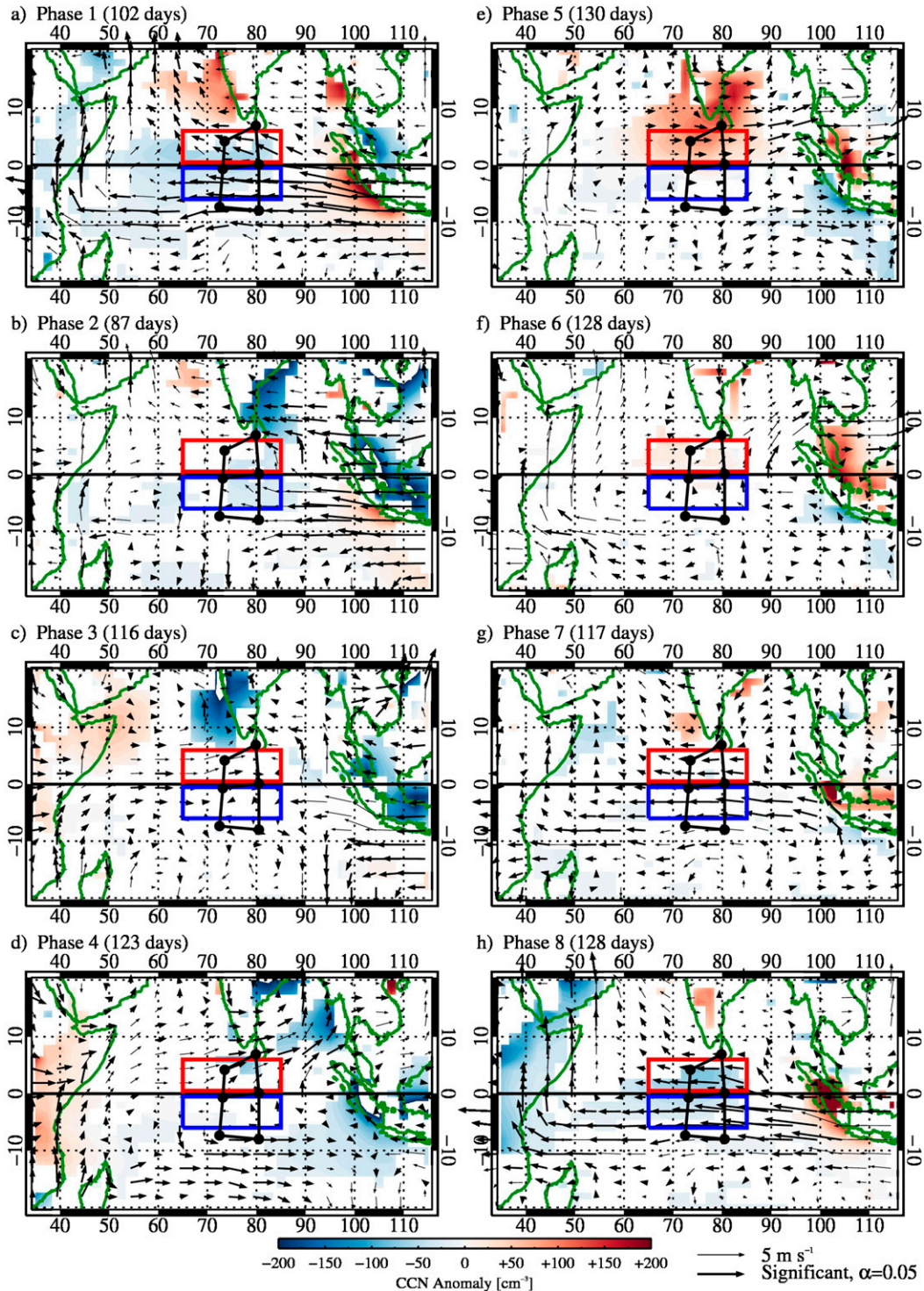


FIG. 7. Composite distributions of the anomaly of boundary layer CCN concentrations (shaded areas denote anomalous CCN concentrations that are statistically significant at the 5% level) as a function of RMM phases 1–8 (the number of days identified for each phase is included above each panel) for cold seasons during the years 2004–11 over the CIO domain (20°S–20°N, 35°–115°E). Composites of the 1000–850-hPa layer-average horizontal wind anomaly at a given point for each RMM phase have been overlaid, scaled by the 5 m s^{-1} black solid vector in the lower right. Anomalous-wind vectors with components that are statistically significant at the 5% level are shown with thick arrows. Outlines of major continents are shown by solid dark green lines. The northern and southern study regions are shown by red and blue solid boxes, respectively, and the northern and southern sounding arrays identified by Johnson and Ciesielski (2013) are shown by black solid lines with dotted vertices.

maximum rainfall occurs over the CIO according to RMM phase diagnostics, anomalous CCN concentrations are generally negative over the CIO and northern and/or southern study regions (the GEOS-Chem model estimates CCN concentrations of $100\text{--}200\text{ cm}^{-3}$ in the northern region and approximately 50 cm^{-3} in the southern region). Meanwhile, in the suppressed periods (RMM phases 4 and 5) an equatorward expansion of the area of polluted continental air is suggested by positive CCN concentration anomalies over India and the adjacent area of ocean in the northern region. During RMM phase 5, actual CCN concentrations exceed more than 500 cm^{-3} in the northern region and CCN concentrations of 100 cm^{-3} extend just south of the equator in CIO.

Weak negative zonal wind anomalies in the lee of India and Sumatra are noted in RMM phases 1, 7, and 8 (Figs. 7a,g,h); in the vicinity of major landmasses, we note a general correspondence between seaward/offshore flow anomalies and enhanced CCN anomalies over adjacent oceans. An exception is found offshore of the western coast of India in RMM phase 5, where anomalous flows oppose the background Asian winter monsoon flow, leading to positive CCN anomalies both locally and over the northern region, in particular. Upon inspection of the 1000–850-hPa layer-mean flow (i.e., not anomalous flow) for RMM phase 5 (not shown), we find enhanced (decreased) equatorward meridional (westward zonal) flow relative to other RMM phases on average, which suggests increased equatorward advection/transport of continental pollutants over the northern CIO to the south of India/Sri Lanka.

Anomalous zonal winds along the equator are among the strongest observed anywhere throughout the CIO domain (roughly -3 to -5 m s^{-1}), regardless of the RMM phase; the peak negative zonal wind anomalies observed in RMM phases 7 and 8 (Figs. 7g,h) are possibly indicative of a Kelvin wave response ahead of the main convective equatorial heat source associated with the MJO (Gill 1980). Positive zonal wind anomalies on the order of 2 m s^{-1} are also noted in RMM phase 3 along the equator, consistent with westerly wind burst episodes that are commonly observed immediately in the wake of active MJO phases in the CIO. Additional aspects of the anomalous patterns shown in Fig. 7 for RMM phases 3–5 (Figs. 7c–e) are also noteworthy in light of results from Gill (1980), particularly the presence of cyclonic flow characteristics in both hemispheres.

Inspection of the anomalous flow pattern in RMM phases 3–5 (Figs. 7c–e) reveals cyclonic turning over parts of the Arabian Sea, India, and the Bay of Bengal, as well as over the southern CIO (poleward of roughly 10°S). We note that the structure of the anomalous flow in RMM phases 3–5 is consistent with the presence of

cyclonic eddies within the larger-scale circulation in the wake of active convective episodes, perhaps evidence of off-equatorial Rossby wave activity (e.g., Gill 1980; Yamagata and Hayashi 1984; Johnson and Ciesielski 2013). Furthermore, the aforementioned climatological evidence for the existence of cyclonic eddies in either hemisphere following active MJO convection in RMM phases 3–5 is consistent with patterns of lower-tropospheric winds observed during DYNAMO following MJOs 2 and 3 (e.g., refer to supplemental materials); recall that “outbreaks” of high CCN concentrations in the northern and southern regions were associated with transient eddies in the wake of the two highlighted MJO episodes from DYNAMO. Thus, there appears to be climatological evidence in support of large-scale flow anomalies maintaining the meridional gradient in CCN between the northern and southern regions of the CIO; hence, we turn to an investigation of the climatological behavior of deep convective clouds in each region (and their respective background environments).

2) THE RESPONSE OF LIGHTNING AND PRECIPITATION TO THE ENVIRONMENT

Figure 8 shows analogous composites of total lightning flash-rate anomalies for each of the eight RMM phases of the MJO cycle, as observed by the TRMM LIS instrument over the wider CIO region. Again, the two-sample Kolmogorov–Smirnov test is used to evaluate the statistical significance of anomalous lightning occurrence (relative to underlying lightning climatology). Even with Gaussian kernel smoothing applied (as described in section 2), the resulting patterns of anomalous lightning observed by TRMM LIS are noisy, likely because of the relatively low frequency of occurrence for observations of strongly electrified convection over the CIO in general. Patterns of anomalous total lightning flash rate suggest increased electrical activity throughout RMM phases 1, 7, and 8 (e.g., Figs. 8a,g,h) and relatively muted lightning activity between RMM phases 3 and 6 (e.g., Figs. 8c–f) over the CIO and surrounding continents. The results presented above in section 3a suggested that lightning observed using the independent set of GLD360 observations during DYNAMO was shown to peak immediately prior to the onset of active phases of the MJO life cycle, especially in the northern region. We find evidence of similar behavior in the spatial composite view and note local positive anomalies downwind of Sumatra in RMM phase 8 and downwind/south of India and Sri Lanka in RMM phase 1, coincident with offshore low-level flows and elevated CCN concentrations. Here, we emphasize that the observed patterns of correspondence do not imply direct causality; future analyses are required in order to determine

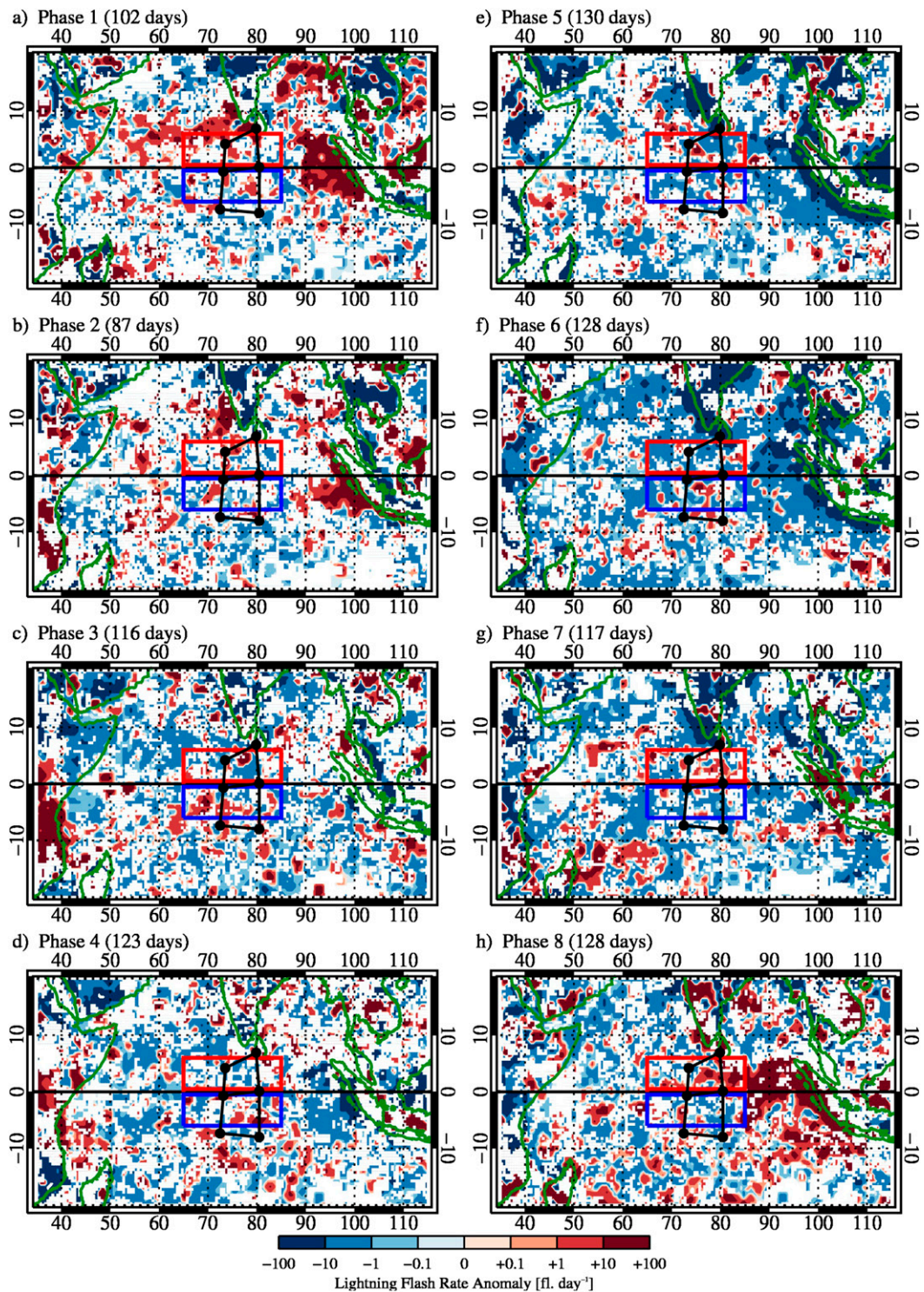


FIG. 8. As in Fig. 7, but for anomalies of daily LIS total lightning flash rate during each RMM phase. Anomalous lightning occurrence is shaded at locations where the anomaly is statistically significant at the 5% level.

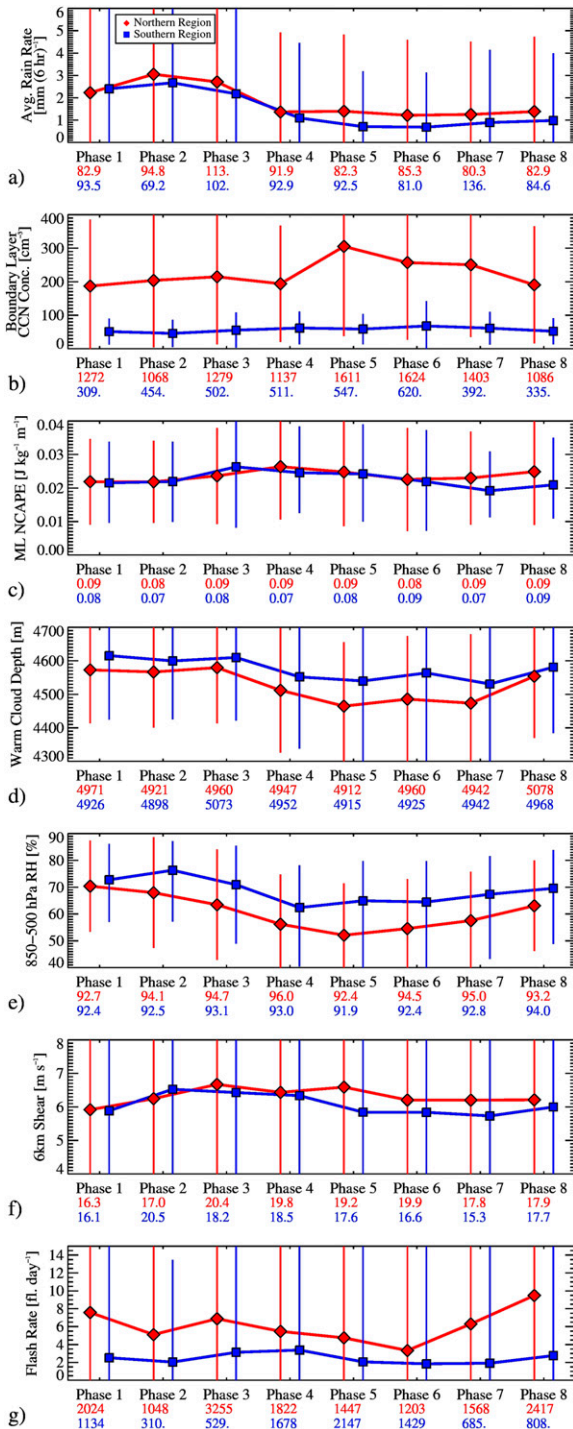


FIG. 9. The RMM-phase composite-mean values of (a) rainfall, (b) CCN concentrations, (c) NCAPE, (d) WCD, (e) 850–500-hPa RH, (f) 6-km shear, and (g) total flash rate between the NR (red) and SR (blue) of the central equatorial Indian Ocean for cold-season months during the years 2004–11. The range of one standard deviation for each parameter in a given RMM phase is shown by the vertical solid lines in colors corresponding to each region. The values below each panel constitute the maximum (minimum) observed values at any point within the corresponding region on any day within each RMM phase for rainfall, CCN concentrations, NCAPE, 850–500-hPa RH, 6-km shear, and total flash rate (WCD).

the individual contributions of CCN and environmental winds (as well as other environmental factors, simultaneously) to the observed patterns of variability in the convective cloud population.

To investigate the temporal evolutionary relationships between average convective cloud behavior, CCN, and environmental factors, we present composites of rainfall, CCN, NCAPE, WCD, midtropospheric RH, vertical wind shear, and total lightning flash rate, following similar composite techniques as above with respect to RMM phase diagnostics (Fig. 9). From these results, it is immediately apparent that there are relationships reminiscent of the patterns seen in observations for the shorter-duration DYNAMO period (Figs. 2, 3). The areal-average rainfall is periodic with peak rain rates observed during RMM phases 2 and 3, and minimum values are observed during suppressed conditions in RMM phases 4–6. A systematic difference (i.e., beyond the noise associated with one standard deviation) in CCN concentrations exists between the northern and southern regions, and periodic variations in CCN are shown for the northern region. CCN concentrations in the northern region are consistently 200 cm^{-3} or more (peaking in RMM phase 5 and diminishing back to the base level thereafter), while CCN concentrations in the southern region stay consistently below 100 cm^{-3} .

In contrast, the difference in NCAPE between regions is generally small, and the magnitude of the areal-mean NCAPE does not vary appreciably throughout the MJO life cycle, on average. WCD and midtropospheric humidity in both regions are periodic, such that RMM phases 1–3 are generally wettest, while suppressed periods during RMM phases 4 and 5 are the driest. Note that WCD is shallower and the midtroposphere is dryer (by about 10% relative humidity), on average, in the northern region compared to the southern region (but the differences between regions do not exceed one standard deviation during a given RMM phase). The magnitude of the 6-km shear vector does not vary more than about 0.5 m s^{-1} through the course of the MJO life cycle in both the northern and the southern regions, but the higher wind shear values generally occur during and after the time when active convection is present in the CIO (i.e., RMM phases 2 and 3). Also consistent with the earlier observations from DYNAMO, composites of lightning observed by TRMM LIS show that lightning flash rate is systematically greater in the northern region compared to the southern region (though, again, the difference between means within a given RMM phase does not exceed one standard deviation). Interestingly, the highest lightning rates in the northern region occur during times where CCN are elevated, yet decreasing,

TABLE 1. Statistics for the number of CFs and LPCFs over the northern and southern regions in the central equatorial Indian Ocean during cold seasons in the 8-yr sample (2004–11). The lower-quartile, median, and upper-quartile values of AVGHT30 and TLD are presented. The mean value of CCN is provided for each of the following subsets of CFs: for all CFs; for all LPCFs; for LPCFs with TLD greater than or equal to the 75th percentile (TLD₇₅); and for CFs with AVGHT30 greater than or equal to the 75th percentile (AVGHT30₇₅).

	Northern region	Southern region
Number of CFs	7142	7522
Number of LPCFs (percentage of CFs)	432 (6.0%)	172 (2.2%)
AVGHT30 (km)	5.5, 6.0, 6.75	5.5, 6.0, 6.5
TLD (flashes min ⁻¹ km ⁻²)	0.000 94, 0.0015, 0.0026	0.000 68, 0.0012, 0.0021
Mean of CCN (for CF; cm ⁻³)	128	57
Mean of CCN (for LPCF; cm ⁻³)	172	82
Mean of CCN (for TLD ₇₅ ; cm ⁻³)	200	79
Mean of CCN (for AVGHT30 ₇₅ ; cm ⁻³)	189	89

when the environment is becoming wetter, and sufficient NCAPE/vertical wind shear exist to sustain the development of deep convection.

We next investigate the potential role of regional differences in CCN (i.e., Fig. 9b) in explaining the variations in the behavior of deep CFs, lightning, and echo-top heights between regions. Table 1 illustrates that there were 7142 CFs in the northern region compared to 7522 CFs in the southern region, and we find median horizontal areas of 700 and 825 km² for CFs in the northern and southern regions, respectively, for the 8-yr cold-season TRMM CF climatology. In the northern region, LPCFs constitute 6.0% (432 LPCFs) of the total CF population observed, compared with just 2.2% (172 LPCFs) of CFs observed in the southern region. Note that the average CCN concentration for both deep CFs and LPCFs is greater in the northern region compared to the southern region by more than a factor of 2. In an effort to study the behavior of the upper extremes of the convective cloud population, we isolate CFs/LPCFs with AVGHT30 and TLD greater than the respective 75th-percentile values for both parameters in each region. We find that the upper quartile of CFs and LPCFs (as defined according to AVGHT30 and TLD percentiles), occur in environments that have progressively higher average CCN concentrations.

To test the dependence of individual convective features on the variations in CCN within a given region, we investigated relationships between each convective intensity metric and CCN for all CFs observed within the span of the cold-season climatology (Fig. 10). From this analysis, we can see that the Spearman rank correlations (*r* values) between the means of convective intensity metrics (e.g., lightning and radar reflectivity echo-top height) and CCN are modest and mostly positive, with the exception of the southern region for lightning density versus CCN in Fig. 10b. The number of LPCFs in the southern region is roughly half of what is observed for the northern region, and Fig. 10b again emphasizes that

LPCFs occur for lower CCN concentrations (CCN < 100 cm⁻³) in that domain. The correlation between lightning and CCN in the southern region is weakly negative, suggesting little discernable impact of variable CCN concentrations for very pristine conditions noted on average in the southern region. While there is quite a bit of variance compared to the mean value in a given bin, the results from the northern region in Fig. 10a suggest that the relationship between total flash density and CCN concentrations is stronger and positive, as lightning increases with increasing CCN once CCN concentrations exceed about 100–200 cm⁻³, consistent with the hypothesis of Rosenfeld et al. (2008). The relationships between the average height of 30-dBZ radar echoes and CCN are very nearly positive monotonic and linear in the northern and southern regions, suggesting first-order dependence of internal precipitation structure on CCN in both regions of the CIO.

For completeness, we studied the frequency of occurrence of VPRR with 30-dBZ echo-top height surpassing incrementally increasing altitude thresholds (Table 2). While the absolute numbers of convective VPRR were larger in the southern region for 30-dBZ echo tops exceeding altitudes less than 5 km, the pattern reverses for convective VPRR with 30-dBZ echo tops exceeding 6 km and greater, such that the deepest 30-dBZ echo tops occur more frequently in the northern region compared to the southern region (by almost a factor of 2 for the highest echo tops). To investigate the possibility that these relationships could be the result of simultaneous correlations with other factors in the environment, we computed the Spearman rank correlation between CCN and NCAPE, WCD, 850–500-hPa RH, and the 6-km wind shear magnitude in turn for each CF in the climatological sample (Table 3). The results of the statistical inquiry illustrate that statistically robust correlations between CCN and other environmental factors are generally less than |0.38|, therefore contributing evidence in support of CCN as a causal factor in explaining

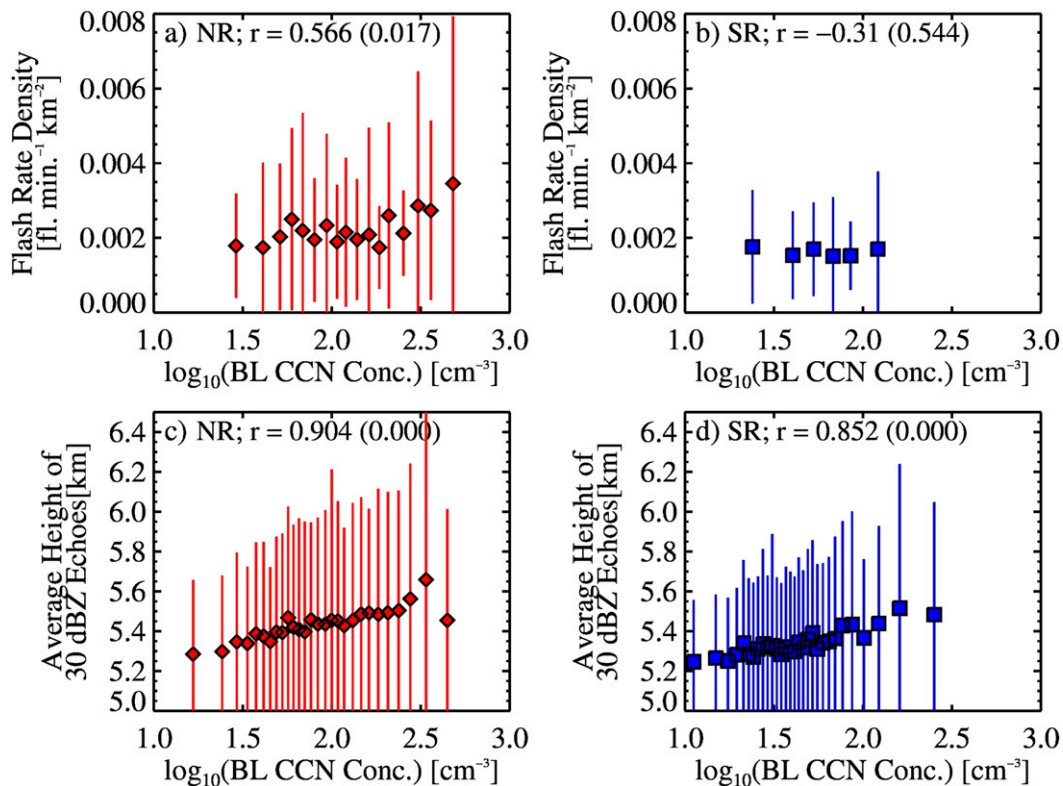


FIG. 10. Relationships between convective intensity metrics for individual convective features/lightning-producing convective features and CCN concentrations during boreal cold-season months for the years 2004–11. The results are separated according to the (a),(c) northern region (red) and (b),(d) southern region (blue) for (a),(b) total lightning density and (c),(d) the average height of 30-dBZ echoes. The mean and resultant standard deviation of convective intensity metrics are shown by filled diamonds (northern region) and filled squares (southern region) and vertical solid bars, respectively, of the corresponding color. The Spearman rank correlation (and associated correlation significance) is denoted at the top of each panel.

regional and temporal variations in the convective cloud population over the CIO (since simultaneous correlations with other factors are weak).

Thus, the results from the climatology indicate that the population of deep CFs in the northern region has slightly higher 30-dBZ echo-top heights, more lightning per unit of convective area, and higher reflectivity at a given altitude (the differences are most pronounced during suppressed phases of the MJO cycle) when compared with the population of deep CFs in the southern region, largely in line with results from the shorter-duration study of observations from DYNAMO in section 3a. While aerosol indirect effects have been implicated for contributing to enhanced internal vertical development of precipitation and greater lightning rates in the northern region during select phases of the intraseasonal cycle, we acknowledge that instability, wind shear, and environmental moisture were sufficient (and perhaps requisite) to allow for deep convection to develop at those times. Therefore, these additional environmental factors likely contribute to the observed

variations of deep convection in the CIO (e.g., Cetrone and Houze 2006; Johnson and Ciesielski 2013; Rowe and Houze 2015). We now turn to a summary of the foregoing results and make concluding remarks.

4. Summary and conclusions

Our results suggest that aerosols advected from the Middle East, India, and southern Asia invigorate convective clouds during certain phases of the MJO, primarily in the northern region of the CIO, via the aerosol-invigoration mechanism described by Rosenfeld et al. (2008). The observations from DYNAMO and climatological results also provide evidence that synoptic-scale, off-equatorial, cyclonic gyres develop in the wake of active MJO convection (e.g., Gill 1980) over the CIO, and these gyres appear to be responsible for reinforcing the background meridional CCN gradient over the CIO; the cyclonic gyres appear to preferentially transport polluted air from the Middle East and southern Asia equatorward after widespread rainfall associated with deep convection

TABLE 2. The absolute numbers of convective VPRR with the maximum height of 30-dBZ echoes (Maxht30) observed by the TRMM PR exceeding specified altitude thresholds in the northern and southern regions of the CIO during cold-season months for the 8-yr (2004–11) climatology.

Maxht30 (km)	Northern region	Southern region
0	334 990	409 624
1	331 119	404 337
2	292 462	350 060
3	224 084	262 826
4	156 474	183 240
5	67 791	74 985
6	18 835	17 130
7	5967	4524
8	2271	1493
9	1022	607
10	501	270

cleanses the atmosphere during previous active phases of the MJO (Figs. 4, 7). Although rainfall and the population of deep convective clouds were found to be comparable between the northern and southern regions of interest, convection developing in more-polluted environments north of the equator produced more lightning compared to convection in pristine environments south of the equator. These results were verified using two independent sets of lightning observations spanning the shorter DYNAMO period (October–December 2011) as well as a climatology of 22 MJO episodes (2004–11).

Convection occurring in polluted environments had higher radar reflectivity in the mixed-phase region (~1–3-dB differences at an altitude of approximately 5–10 km). We emphasize that average NCAPE did not vary appreciably between the northern and southern regions, while environmental humidity and CCN were shown to vary considerably between regions and, to a lesser extent, throughout the different RMM phases of the MJO episodes documented in the 8-yr cold-season climatology. Maxima in spatial RMM composite distributions of total lightning from the cold-season climatology (2004–11) in the northern region of the CIO were associated with seaward/equatorward advection of continental CCN. Important results from this study are 1) that deep convective features with 30-dBZ echo tops

exceeding 6, 7, 8, 9, and 10 km occur more frequently in the northern region than in the southern region and were strongly correlated with CCN at the level of individual convective features and 2) that total lightning was more frequent and more intense coincidentally in time with elevated (yet diminishing) CCN concentrations and increasing column moisture primarily in the northern CIO. Our results are consistent with the hypothesis that increased CCN concentrations, as a result of advection from nearby continents (e.g., Fig. 7), are responsible for differences in convective intensity over the CIO (Figs. 2, 4 and Figs. 8, 9), superposed on an environment in which instability, moisture, and vertical wind shear support the development of deep convection during preferred (i.e., preonset) phases of the MJO cycle.

Specifically in the tropics, the vertical wind shear in the lower and midtroposphere has been shown to strongly influence convective cloud morphology, dimension, and cloud lifetime, subsequently impacting the vertical mass flux, cold pool dynamics, and secondary convective development (LeMone et al. 1998; Cetrone and Houze 2006; Rowe and Houze 2015). The spatial dimensions and vigor of convective updrafts have been cited as key cloud attributes for determining to what extent entrainment and mixing processes can impact a cloudy parcel's buoyancy (e.g., Williams and Stanfill 2002). The efficacy of entrainment/mixing processes to dilute convective updrafts is also likely to be sensitive to the ambient humidity of the free troposphere.

In turn, both wind shear and free-tropospheric relative humidity have been shown to vary considerably during various phases of the MJO in previous studies (Johnson and Ciesielski 2013; Xu and Rutledge 2014; Rowe and Houze 2015), with both wind shear and column moisture peaking during and just after the development of widespread precipitation in active convective phases of the MJO. Grant and van den Heever (2015) and the results from earlier studies referenced therein have suggested that, for convective clouds developing in the presence of high CCN concentrations, smaller hydrometeor diameters and greater overall surface area in the collective population of hydrometeors promotes stronger evaporative cooling/downrafts and

TABLE 3. The Spearman rank correlations for relationships between CCN and mixed-layer NCAPE, WCD, 850–500-hPa average RH, and the 6-km shear vector (SHEAR) attributed to convective features observed within the northern and southern regions of the CIO (6°S–6°N, 65°–85°E) for the years 2004–11. The two-tailed significance values associated with each Spearman rank correlation are provided in parentheses. See section 2c for description of CF database and attribution methodology.

	NCAPE	WCD	RH	SHEAR
Northern region	0.062 (0.000)	−0.171 (0.000)	−0.328 (0.000)	−0.062 (0.000)
Southern region	0.151 (0.000)	−0.188 (0.000)	−0.377 (0.000)	−0.034 (0.003)

subsequently stronger secondary convection. Thorough investigation of these phenomena would require a detailed depiction of numerous convective clouds and their respective environments as well as a stringent statistical method designed to isolate the relative contributions of individual environmental factors to the observed variability of deep convective clouds. We leave such analyses to future work for the sake of brevity in the current investigation.

Previous studies depicting regional differences in lightning over oceanic regions for approximately 1–3-dB differences in reflectivity and variable CCN concentrations highlight the need for more-detailed studies of microphysical behavior within deep convective clouds as a function of environmental CCN concentrations and the environmental factors studied here (e.g., conditional instability, vertical wind shear, and lower-/midtropospheric moisture), especially in coastal regions. Global (cloud resolving) model studies incorporating the influence of aerosols on the microphysics of deep convection will be necessary to examine more specific aspects of hypotheses for the role of aerosols as they impact convective clouds in the CIO during various phases of the MJO. Additionally, it is of interest to know whether characteristics of individual episodes of the MJO (e.g., MJO onset and the duration/intensity of widespread rainfall) are sensitive to the initial distributions of CCN and the magnitude of the cross-equatorial meridional gradient in CCN.

Acknowledgments. We are grateful to three anonymous reviewers for their criticism and thoughtful suggestions. The authors wish to thank Vaisala, Inc., for providing continuous lightning observations and technical support for their data. We acknowledge S. Farina and P. Hein for their assistance in technical computing. Information about the GEOS-Chem (www.geos-chem.org) with the online TOMAS aerosol microphysics module is available online (http://wiki.seas.harvard.edu/geos-chem/index.php/TOMAS_aerosol_microphysics). Output from the GEOS-Chem simulations analyzed in this study is available by special request (dstolz@atmos.colostate.edu). Global reanalysis [Modern-Era Retrospective Analysis for Research and Applications (MERRA)] and data from the Tropical Rainfall Measuring Mission satellite are available from National Aeronautics and Space Administration (NASA) servers via the Global Modeling and Assimilation Office (<http://gmao.gsfc.nasa.gov/merra/>) and the Goddard Earth Sciences Data and Information Services Center (<http://disc.sci.gsfc.nasa.gov/TRMM>). This research was supported by the National Science Foundation AGS Grant 1063928 and NASA PMM Grant NNX13AG32G.

APPENDIX

Index of Terms

CAPE	Convective available potential energy
CCF	Cold cloud feature
CCN	Cloud condensation nuclei
CF	Convective feature
CIO	Central Indian Ocean
DYNAMO	Dynamics of the Madden–Julian Oscillation field campaign
EOF	Empirical orthogonal function
GLD360	Global Lightning Dataset (Vaisala)
INDOEX	Indian Ocean Experiment
IR	Infrared
LCL	Lifting condensation level
LIS	TRMM Lightning Imaging Sensor
LPCF	Lightning-producing convective feature
MERRA	Modern-Era Retrospective Analysis for Research and Applications
MJO	Madden–Julian oscillation
N40	Number concentration of particles with diameters larger than 40 nm
NCAPE	Normalized convective available potential energy
PR	TRMM Precipitation Radar
RMM	Real-Time Multivariate MJO index (Wheeler and Hendon 2004)
TRMM	Tropical Rainfall Measuring Mission
VPRR	Vertical profile of radar reflectivity

REFERENCES

- Adams, P. J., and J. H. Seinfeld, 2002: Predicting global aerosol size distributions in general circulation models. *J. Geophys. Res.*, **107**, 4370, doi:10.1029/2001JD001010.
- Arkin, P. A., 1979: The relationship between fractional coverage of high cloud and rainfall accumulations during GATE over the B-scale array. *Mon. Wea. Rev.*, **107**, 1382–1387, doi:10.1175/1520-0493(1979)107<1382:TRBFCO>2.0.CO;2.
- Bates, T. S., D. J. Coffman, D. S. Covert, and P. K. Quinn, 2002: Regional marine boundary layer aerosol size distributions in the Indian, Atlantic, and Pacific Oceans: A comparison of INDOEX measurements with ACE-1, ACE-2, and Aerosols99. *J. Geophys. Res.*, **107**, 8026, doi:10.1029/2001JD001174.
- Beegum, S. N., K. Krishna Moorthy, S. S. Babu, R. R. Reddy, and K. R. Gopal, 2009: Large scale modulations of spectral aerosol optical depths by atmospheric planetary waves. *Geophys. Res. Lett.*, **36**, L03810, doi:10.1029/2008GL036509.
- Boccippio, D. J., S. J. Goodman, and S. Heckman, 2000: Regional differences in tropical lightning distributions. *J. Appl. Meteor.*, **39**, 2231–2248, doi:10.1175/1520-0450(2001)040<2231:RDITLD>2.0.CO;2.
- Carey, L. D., and K. M. Buffalo, 2007: Environmental control of cloud-to-ground lightning polarity in severe storms. *Mon. Wea. Rev.*, **135**, 1327–1353, doi:10.1175/MWR3361.1.

- Cecil, D. J., D. E. Buechler, and R. J. Blakeslee, 2014: Gridded lightning climatology from TRMM-LIS and OTD: Dataset description. *Atmos. Res.*, **135–136**, 404–414, doi:10.1016/j.atmosres.2012.06.028.
- Cetrone, J., and R. A. Houze Jr., 2006: Characteristics of tropical convection over the ocean near Kwajalein. *Mon. Wea. Rev.*, **134**, 834–853, doi:10.1175/MWR3075.1.
- Ciesielski, P. E., and Coauthors, 2014: Quality-controlled upper-air sounding dataset for DYNAMO/CINDY/AMIE: Development and corrections. *J. Atmos. Oceanic Technol.*, **31**, 741–764, doi:10.1175/JTECH-D-13-00165.1.
- D'Andrea, S. D., and Coauthors, 2013: Understanding global secondary organic aerosol amount and size-resolved condensational behavior. *Atmos. Chem. Phys.*, **13**, 11 519–11 534, doi:10.5194/acp-13-11519-2013.
- Dusek, U., and Coauthors, 2006: Size matters more than chemistry for cloud-nucleating ability of aerosol particles. *Science*, **312**, 1375–1378, doi:10.1126/science.1125261.
- Field, R. D., G. R. van der Werf, and S. S. P. Shen, 2009: Human amplification of drought-induced biomass burning in Indonesia since 1960. *Nat. Geosci.*, **2**, 185–188, doi:10.1038/ngeo443.
- Gill, A. E., 1980: Some simple solutions for heat-induced tropical circulation. *Quart. J. Roy. Meteor. Soc.*, **106**, 447–462, doi:10.1002/qj.49710644905.
- Gottschalck, J., P. E. Roundy, C. J. Schreck III, A. Vintzileos, and C. Zhang, 2013: Large-scale atmospheric and oceanic conditions during the 2011–12 DYNAMO field campaign. *Mon. Wea. Rev.*, **141**, 4173–4196, doi:10.1175/MWR-D-13-00022.1.
- Grant, L. D., and S. C. van den Heever, 2015: Cold pool and precipitation responses to aerosol loading: Modulation by dry layers. *J. Atmos. Sci.*, **72**, 1398–1408, doi:10.1175/JAS-D-14-0260.1.
- Guo, Y., B. Tian, R. A. Kahn, O. Kalashnikova, S. Wong, and D. E. Waliser, 2013: Tropical Atlantic dust and smoke aerosol variations related to the Madden–Julian oscillation in MODIS and MISR observations. *J. Geophys. Res. Atmos.*, **118**, 4947–4963, doi:10.1002/jgrd.50409.
- Heintzenberg, J., D. C. Covert, and R. Vandingenen, 2000: Size distribution and chemical composition of marine aerosols: A compilation and review. *Tellus*, **52B**, 1104–1122, doi:10.1034/j.1600-0889.2000.00136.x.
- Huffman, G. J., and Coauthors, 2007: The TRMM Multisatellite Precipitation Analysis (TMPA): Quasi-global, multiyear, combined sensor precipitation estimates at fine scales. *J. Hydrometeorol.*, **8**, 38–55, doi:10.1175/JHM560.1.
- Iguchi, T., T. Kozu, R. Meneghini, J. Awaka, and K. Okamoto, 2000: Rain-profiling algorithm for the TRMM precipitation radar. *J. Appl. Meteor.*, **39**, 2038–2052, doi:10.1175/1520-0450(2001)040<2038:RPAFTT>2.0.CO;2.
- Iribarne, J. V., and W. L. Godson, 1981: *Atmospheric Thermodynamics*. 2nd ed. D. Reidel Publishing Co., 244 pp.
- Johnson, R. H., and P. E. Ciesielski, 2013: Structure and properties of Madden–Julian oscillations deduced from DYNAMO sounding arrays. *J. Atmos. Sci.*, **70**, 3157–3179, doi:10.1175/JAS-D-13-065.1.
- Kiladis, G. N., K. H. Straub, and P. T. Haertel, 2005: Zonal and vertical structure of the Madden–Julian oscillation. *J. Atmos. Sci.*, **62**, 2790–2809, doi:10.1175/JAS3520.1.
- , J. Dias, K. H. Straub, M. C. Wheeler, S. N. Tulich, K. Kikuchi, K. M. Weickmann, and M. J. Ventrice, 2014: A comparison of OLR and circulation-based indices for tracking the MJO. *Mon. Wea. Rev.*, **142**, 1697–1715, doi:10.1175/MWR-D-13-00301.1.
- Krishnamurti, T. N., B. Jha, J. Prospero, A. Jayaraman, and V. Ramanathan, 1998: Aerosol and pollutant transport and their impact on radiative forcing over the tropical Indian Ocean during the January–February 1996 pre-INDOEX cruise. *Tellus*, **50B**, 521–542, doi:10.1034/j.1600-0889.1998.00009.x.
- Kummerow, C., W. Barnes, T. Kozu, J. Shiue, and J. Simpson, 1998: The Tropical Rainfall Measuring Mission (TRMM PR) sensor package. *J. Atmos. Oceanic Technol.*, **15**, 809–817, doi:10.1175/1520-0426(1998)015<0809:TTRMMT>2.0.CO;2.
- Langley DeWitt, H., D. J. Coffman, K. J. Schulz, W. Alan Brewer, T. S. Bates, and P. K. Quinn, 2013: Atmospheric aerosol properties over the equatorial Indian Ocean and the impact of the Madden–Julian oscillation. *J. Geophys. Res. Atmos.*, **118**, 5736–5749, doi:10.1002/jgrd.50419.
- Lau, K., and P. H. Chan, 1986: Aspects of the 40–50 day oscillation during the northern summer as inferred from outgoing longwave radiation. *Mon. Wea. Rev.*, **114**, 1354–1367, doi:10.1175/1520-0493(1986)114<1354:AOTDOD>2.0.CO;2.
- LeMone, M. A., E. J. Zipser, and S. B. Trier, 1998: The role of environmental shear and thermodynamic conditions in determining the structure and evolution of mesoscale convective systems during TOGA COARE. *J. Atmos. Sci.*, **55**, 3493–3518, doi:10.1175/1520-0469(1998)055<3493:TROESA>2.0.CO;2.
- Li, F., and V. Ramanathan, 2002: Winter to summer monsoon variation of aerosol optical depth over the tropical Indian Ocean. *J. Geophys. Res.*, **107**, 4284, doi:10.1029/2001JD000949.
- Liu, C., E. J. Zipser, D. J. Cecil, S. W. Nesbitt, and S. Sherwood, 2008: A cloud and precipitation feature database from nine years of TRMM observations. *J. Appl. Meteor. Climatol.*, **47**, 2712–2728, doi:10.1175/2008JAMC1890.1.
- Madden, R. A., 1986: Seasonal variations of the 40–50 day oscillation in the tropics. *J. Atmos. Sci.*, **43**, 3138–3158, doi:10.1175/1520-0469(1986)043<3138:SVOTDO>2.0.CO;2.
- , and P. R. Julian, 1971: Detection of a 40–50 day oscillation in the zonal wind in the tropical Pacific. *J. Atmos. Sci.*, **28**, 702–708, doi:10.1175/1520-0469(1971)028<0702:DOADOI>2.0.CO;2.
- , and —, 1972: Description of global-scale circulation cells in the tropics with a 40–50 day period. *J. Atmos. Sci.*, **29**, 1109–1123, doi:10.1175/1520-0469(1972)029<1109:DOGSCC>2.0.CO;2.
- , and —, 1994: Observations of the 40–50-day tropical oscillation—A review. *Mon. Wea. Rev.*, **122**, 814–837, doi:10.1175/1520-0493(1994)122<0814:OOTDIO>2.0.CO;2.
- Mapes, B. E., and R. A. Houze Jr., 1993: Cloud clusters and superclusters over the oceanic warm pool. *Mon. Wea. Rev.*, **121**, 1398–1416, doi:10.1175/1520-0493(1993)121<1398:CCASOT>2.0.CO;2.
- Moorthy, K. K., and A. Saha, 2000: Aerosol study during INDOEX: Observation of enhanced aerosol activity over the mid Arabian Sea during the northern winter. *J. Atmos. Sol.-Terr. Phys.*, **62**, 65–72, doi:10.1016/S1364-6826(99)00081-4.
- Nesbitt, S. W., E. J. Zipser, and D. J. Cecil, 2000: A census of precipitation features in the tropics using TRMM: Radar, ice scattering, and lightning observations. *J. Climate*, **13**, 4087–4106, doi:10.1175/1520-0442(2000)013<4087:ACOPFI>2.0.CO;2.
- Pierce, J. R., and P. J. Adams, 2009: Uncertainty in global CCN concentrations from uncertain aerosol nucleation and primary emission rates. *Atmos. Chem. Phys.*, **9**, 1339–1356, doi:10.5194/acp-9-1339-2009.
- , M. J. Evans, C. E. Scott, S. D. D'Andrea, D. K. Farmer, E. Sweitlicki, and D. V. Spracklin, 2013: Weak global sensitivity of cloud condensation nuclei and the aerosol indirect effect to Criegee + SO₂ chemistry. *Atmos. Chem. Phys.*, **13**, 3163–3176, doi:10.5194/acp-13-3163-2013.
- Ramanathan, V., and Coauthors, 2001: Indian Ocean Experiment: An integrated analysis of the climate forcing and effects of the great Indo-Asian haze. *J. Geophys. Res.*, **106**, 28 371–28 398, doi:10.1029/2001JD900133.

- Reid, J. S., and Coauthors, 2012: Multi-scale meteorological conceptual analysis of observed active fire hotspot activity and smoke optical depth in the Maritime Continent. *Atmos. Chem. Phys.*, **12**, 2117–2147, doi:10.5194/acp-12-2117-2012.
- Rosenfeld, D., R. Lahav, A. Khain, and M. Pinsky, 2002: The role of sea spray in cleansing air pollution over ocean via cloud processes. *Science*, **297**, 1667–1670, doi:10.1126/science.1073869.
- , U. Lohmann, G. B. Raga, C. D. O'Dowd, M. Kulmala, S. Fuzzi, A. Reissell, and M. O. Andreae, 2008: Flood or drought: How do aerosols affect precipitation? *Science*, **321**, 1309–1313, doi:10.1126/science.1160606.
- , and Coauthors, 2014: Global observations of aerosol–cloud–precipitation climate interactions. *Rev. Geophys.*, **52**, 750–808, doi:10.1002/2013RG000441.
- Rowe, A. K., and R. A. Houze Jr., 2015: Cloud organization and growth during the transition from suppressed to active MJO conditions. *J. Geophys. Res. Atmos.*, **120**, 10 324–10 350, doi:10.1002/2014JD022948.
- Satheesh, S. K., K. K. Moorthy, and B. V. K. Murthy, 1998: Spatial gradients in aerosol characteristics over the Arabian Sea and Indian Ocean. *J. Geophys. Res.*, **103**, 26 183–26 192, doi:10.1029/98JD00803.
- , V. Ramanathan, X. Li-Jones, J. M. Lobert, I. A. Podgorny, J. M. Prospero, B. N. Holben, and N. G. Loeb, 1999: A model for the natural and anthropogenic aerosols over the tropical Indian Ocean derived from Indian Ocean Experiment data. *J. Geophys. Res.*, **104**, 27 421–27 440, doi:10.1029/1999JD900478.
- Saunders, C. P. R., 1993: A review of thunderstorm electrification processes. *J. Appl. Meteor.*, **32**, 642–655, doi:10.1175/1520-0450(1993)032<0642:AROTEP>2.0.CO;2.
- Spracklen, D. V., K. S. Carslaw, U. Poschl, A. Rap, and P. M. Forster, 2011: Global cloud condensation nuclei influenced by carbonaceous combustion aerosol. *Atmos. Chem. Phys.*, **11**, 9067–9087, doi:10.5194/acp-11-9067-2011.
- Stephens, G. L., P. J. Webster, R. H. Johnson, R. Engelen, and T. S. L'Ecuyer, 2004: Observational evidence for the mutual regulation of the tropical hydrological cycle and tropical sea surface temperatures. *J. Climate*, **17**, 2213–2224, doi:10.1175/1520-0442(2004)017<2213:OEFTMR>2.0.CO;2.
- Stolz, D. C., S. A. Rutledge, and J. R. Pierce, 2015: Simultaneous influences of thermodynamics and aerosols on deep convection and lightning in the tropics. *J. Geophys. Res. Atmos.*, **120**, 6207–6231, doi:10.1002/2014JD023033.
- Storer, R. L., and S. C. van den Heever, 2013: Microphysical processes evident in aerosol forcing of tropical deep convective clouds. *J. Atmos. Sci.*, **70**, 430–446, doi:10.1175/JAS-D-12-076.1.
- , —, and T. S. L'Ecuyer, 2014: Observations of aerosol-induced convective invigoration in the tropical east Atlantic. *J. Geophys. Res. Atmos.*, **119**, 3963–3975, doi:10.1002/2013JD020272.
- Straub, K. H., 2013: MJO initiation in the real-time multivariate MJO index. *J. Climate*, **26**, 1130–1151, doi:10.1175/JCLI-D-12-00074.1.
- Tao, W.-K., J.-P. Chen, Z. Li, C. Wang, and C. Zhang, 2012: Impact of aerosols on convective clouds and precipitation. *Rev. Geophys.*, **50**, RG2001, doi:10.1029/2011RG000369.
- Tian, B., and Coauthors, 2008: Does the Madden–Julian oscillation influence aerosol variability? *J. Geophys. Res.*, **113**, D12215, doi:10.1029/2007JD009372.
- , D. E. Waliser, R. A. Kahn, and S. Wong, 2011: Modulation of Atlantic aerosols by the Madden–Julian oscillation. *J. Geophys. Res.*, **116**, D15108, doi:10.1029/2010JD015201.
- Wall, C., E. Zipser, and C. Liu, 2014: An investigation of the aerosol indirect effect on convective intensity using satellite observations. *J. Atmos. Sci.*, **71**, 430–447, doi:10.1175/JAS-D-13-0158.1.
- Wheeler, M., and H. H. Hendon, 2004: An all-season Real-Time Multivariate MJO index: Development of an index for monitoring and prediction. *Mon. Wea. Rev.*, **132**, 1917–1932, doi:10.1175/1520-0493(2004)132<1917:AARMMI>2.0.CO;2.
- Wilks, D. S., 2011: *Statistical Methods in the Atmospheric Sciences*. 3rd ed. Academic Press, 704 pp.
- Williams, E. R., and S. Stanfill, 2002: The physical origin of the land–ocean contrast in lightning activity. *C. R. Phys.*, **3**, 1277–1292, doi:10.1016/S1631-0705(02)01407-X.
- , T. V. Mushtak, D. Rosenfeld, S. Goodman, and D. Boccippio, 2005: Thermodynamic conditions favorable to superlative thunderstorm updraft, mixed phase microphysics and lightning flash rate. *Atmos. Res.*, **76**, 288–306, doi:10.1016/j.atmosres.2004.11.009.
- Xu, W., and S. A. Rutledge, 2014: Convective characteristics of the Madden–Julian oscillation over the central Indian Ocean observed by shipborne radar during DYNAMO. *J. Atmos. Sci.*, **71**, 2859–2877, doi:10.1175/JAS-D-13-0372.1.
- , and —, 2015: Morphology, intensity, and rainfall production of MJO convection: Observations from DYNAMO shipborne radar and TRMM. *J. Atmos. Sci.*, **72**, 623–640, doi:10.1175/JAS-D-14-0130.1.
- , —, C. Schumacher, and M. Katsumata, 2015: Evolution, properties, and spatial variability of MJO convection near and off the equator during DYNAMO. *J. Atmos. Sci.*, **72**, 4126–4147, doi:10.1175/JAS-D-15-0032.1.
- Yamagata, T., and Y. Hayashi, 1984: A simple diagnostic model for the 30–50 day oscillation in the Tropics. *J. Meteor. Soc. Japan*, **62**, 709–717.
- Yoneyama, K., C. Zhang, and C. N. Long, 2013: Tracking pulses of the Madden–Julian oscillation. *Bull. Amer. Meteor. Soc.*, **94**, 1871–1891, doi:10.1175/BAMS-D-12-00157.1.
- Zhang, C., 2005: Madden–Julian oscillation. *Rev. Geophys.*, **43**, RG2003, doi:10.1029/2004RG000158.
- , 2013: Madden–Julian oscillation: Bridging weather and climate. *Bull. Amer. Meteor. Soc.*, **94**, 1849–1870, doi:10.1175/BAMS-D-12-00026.1.
- , and M. Dong, 2004: Seasonality in the Madden–Julian oscillation. *J. Climate*, **17**, 3169–3180, doi:10.1175/1520-0442(2004)017<3169:SITMO>2.0.CO;2.